High-energy SWCNT cathode for aqueous Al-ion battery boosted by multi-ion intercalation chemistry

High-Energy SWCNT Cathode for Aqueous Al-ion Battery Boosted by Multi-ion Intercalation Chemistry

Wending Pan, Yan Zhao, Jianjun Mao, Yifei Wang, Xiaolong Zhao, Kee Wah Leong, Shijing Luo, Xinhua Liu, Huizhi Wang, Jin Xuan, Shichun Yang, Yue Chen, D.Y.C Leung**

W. D. Pan, J.J. Mao, X. L. Zhao, K. W. Leong, S. J. Luo, Prof. D.Y.C Leung
Department of Mechanical Engineering, the University of Hong Kong, 999077, China.
E-mail: ycleung@hku.hk

Dr. X. H. Liu, Prof. S. C. Yang
School of Transportation Science and Engineering, Beihang University, Beijing 100083, China.
E-mail: liuxinhua19@buaa.edu.cn

Dr. Y. Zhao, Dr. H. Z. Wang
Department of Mechanical Engineering, Imperial College London, SW7 2AZ, UK.

Dr. Y. F. Wang
School of Mechanical Engineering and Automation, Harbin Institute of Technology, Shenzhen, 518055, China.

Prof. J. Xuan
Department of Chemical Engineering, Loughborough University, Loughborough LE11 3TU, UK.

Keywords: Aqueous Al-ion battery, SWCNT cathode, High-capacity cathode, Multi-ion intercalation chemistry, Cl-assisted intercalation.

Abstract: The aqueous Al-ion battery has achieved great progress in recent years so that it shows comparable performance to that of even non-aqueous Al-ion batteries. However, it also shows relatively low energy output and a limited general understanding of the mechanism behind it restricting its practical application. Thus, the development of high-performance cathode material is in great demand. Herein, a high-capacity single-walled carbon nanotube (SWCNT) was developed as cathode for the water-in-salt electrolyte-based aqueous Al-ion battery, which provided an ultra-high specific capacity of 790 mAh g^{-1} (based on the mass of SWCNT) at a high current density of 5A g^{-1} even after 1000 cycles. Moreover, the SWCNT/Al battery showed a complicated multi-ion intercalation mechanism, where $AlCl_4^-$, Cl^-, Al^{3+} and H^+ can function at the same time, promoting the battery output. Beyond recently revealed H^+ and metal ion co-intercalation, Cl-assisted intercalation of Al^{3+} ions mechanism was also studied by experimental characterization and modelling for the first time, which significantly boosted the Al storage capacity. This multi-ion intercalation mechanism

combines the high-voltage anion deintercalation and the high-capacity cation intercalation, and thus, benefits the development and application of high-energy Al-ion batteries in the future.

1. Introduction

Shortage and environmental pollution of fossil fuels have long been a concern for modern society, thus it is in great demand to utilize renewable resources, such as solar and wind energy. To use these new energy resources effectively, energy storage techniques are crucial and rechargeable ion battery technology is one of the most developed energy storage technologies, which shows a very promising future. Although Li-ion batteries have achieved significant success, the high price of lithium metal and safety issues restrict its further development. Aluminium ion battery (AIB) is regarded as one of the most promising candidates for the post-Li-ion battery era, due to its low cost and high theoretical capacity. Although the ionic liquid electrolyte based AIB achieved a high operation voltage with high stability, it faces many problems, such as low capacity and high-cost electrolytes. Aqueous aluminium ion battery (AAIB) takes the advantage of AIB and avoid the expensive electrolyte of non-aqueous AIB, showing promising potential for practical applications. Among all the AAIBs, water-in-salt state (WIS) AAIB achieved comparable performance with non-aqueous AIBs, which successfully expanded the electrochemical window of the aqueous system, delivering a high discharge capacity of 200 mAh g^{-1} and a high discharge plateau voltage of 1.8V. However, the capacity of the cathode material is limited compared with the high capacity of 2980 mAh g^{-1} of Al metal anode theoretically. Thus, it is demanded to promote the output of WIS-AAIB.

Carbon materials show a bright future as high-performance cathode for AAIBs, with graphite and 2D structured graphene widely utilized in recently reported AIBs. Lin et al. [1] firstly assembled an ionic liquid electrolyte based graphite/Al battery, showing the ultrafast charge/discharge ability with high stability over 7500 cycles. After that, a series of studies on Al-ion batteries have been conducted, and the average voltage plateau of the graphite/Al battery system has been promoted to 1.8V[2-3]. As a novel 2D material, graphene has also been studied as cathode material for AIBs recently[4]. Chen et al. demonstrated a graphene/Al battery[5], of which the cyclability and power density were boosted, delivering a high capacity retention of 98% after 25000 cycles at a high current density of 5A g^{-1}. However, although it still shows a limited discharge capacity of around 120 mAh g^{-1}. Thus, the carbon material for AIBs demands further development, especially for higher discharge capacity. Among all

carbon materials, 1D carbon material, e.g., carbon nanotube (CNT), has not been studied thoroughly for Al ion storage. Traditionally, CNTs were utilized in a variety of ways ranging from conductive additives, current collectors, and active materials for Li-ion batteries. Among different CNTs, the unique electrochemical and mechanical properties of single-walled carbon nanotube (SWCNT) make it potential for use in high energy density Li-ion batteries. A high theoretical specific capacity of more than 1116 mAh g^{-1} for Li ion storage has been theoretically calculated due to the abundant interstitial sites on the nanotube surface, inside the individual nanotubes, and between the respective SWCNTs in the close-packed bundles[6]. Experimentally, Ziat et al. achieved a high capacity of 1200 mAh^{-1} by a 1.75nm-diameter-wide SWCNT, confirming the high capacity of SWCNT[7]. Moreover, SWCNT also shows a high OCV of 2.8V[8] for Na-ion batteries, showing the promising future of CNT-based high-performance ion batteries. Theoretically, the triple-valent Al^{3+} ion can provide much higher performance than that of monovalent Li^{+} ion, however, only a few investigations on CNT cathode has been conducted for AAIBs[9].

Besides, the complicated ion intercalation chemistry of AAIB has not been revealed thoroughly. Compared with sole intercalation ion in ionic liquid ([EMIm]Cl-$AlCl_3$) based Al-ion battery, e.g., $AlCl_4^-$, and organic electrolyte ($Al(OTf)_3$) based[10-11], e.g., Al^{3+}, multi-ion can be regarded as active electrochemical species in non-organic aqueous electrolyte system[12-14], for example, $AlCl_4^-$, Al^{3+}, Cl^- and H^+ co-exists in WIS-$AlCl_3$ electrolyte[15], which contribute a lot to the discharge capacity. Thus, the mechanism behind the multi-ion intercalation behaviour needs to be further studied as the interaction of these ions may affect the battery performance greatly.

Herein, a high-capacity SWCNT/Al battery was reported, which achieved a record-breaking discharge capacity of 790 mAh g^{-1} (based on the mass of SWCNT) with two discharge plateaus at 1.8V and 1.2V, contributing to a high energy density of 980 Wh kg^{-1}. The cathode was also found to have high stability with more than 1000 cycles at a high current density of 5A g^{-1}. More importantly, multi-ion intercalation chemistry was revealed: besides a high discharge voltage plateau at 1.8V for $AlCl_4^-$ de-intercalation, the Cl^- ion was found to play an important role for Al^{3+}/H^+ ion co-intercalation, enabling a promoted discharge plateau capacity at 1.2V.

2. Results and discussion

2.1 Preparation of SWCNT cathode and characterization

The single-walled carbon nanotube (SWCNT) with carboxymethyl cellulose (CMC) additive was directly utilized as cathode material without further processing. Its structure and degree of graphitization were characterized by Raman spectroscopy (Figure 1a), where almost neglectable D band wavelength could be detected, suggesting the limited defects in the SWCNT. This is consistent with the $AlCl_4^-$ intercalation favoured "defect-free" feature proposed by Chen et al. [5]. The radical beam mode (RBM) region indicates the diameter of the SWCNT is around 0.89nm (267cm^{-1}) and 1.31nm (186cm^{-1}). Its surface groups were also examined by Fourier transform infrared (FTIR) spectroscopy (Figure 1b). Besides signals of C-C-C and C=C bonds[16], some oxygen-containing groups, such as C-O-H and C=O [17], were found, which may result from functionalized SWCNT surface and additive CMC binder. The micromorphology of the SWCNT was observed by scanning electron microscope (SEM, Figure S1a-c), where its length of several micrometres to even tens of micrometres can be seen. A closer look of SWCNT was shown by high-resolution transmission electron microscopy (HRTEM, Figure 1c and Figure S1d), where the SWCNT bundle (mostly with a diameter of 10 nm) was found, which consists of several single SWCNTs, and the diameter of a single SWCNT can be determined to be around 1nm, corresponding to the RBM mode signal of Raman spectra (Figure 1a). As the agglomeration state is an important factor for the SWCNT bundles, it was further studied and labelled in Figure S1 c and d, which shows a uniform distribution of the bundle size around 15 nm, although some large bundles can reach a large size of 40 nm and some single SWCNTs still exist. The uniform distribution of the bundle size can contribute to the consistency of the electrochemical performance. Compared with large-diameter multi-walled carbon nanotubes (MWCNT, Figure S2), it is evident that the small-diameter SWCNT shows a large electrochemically active surface area, which can provide more potential interstitial sites. The crystal lattice of SWCNT was further observed by selected area electron diffraction (SAED, Figure 1d), where it is indexed to the standard pattern of carbon material and the (002) and (110) facet shows the highest intensity.

2.2 Electrochemical performance of the SWCNT cathode

Owing to the unique structure of SWCNT cathode, the SWCNT/Al AAIB shows an excellent discharge capacity of 690 mAh g^{-1} (corresponding to an energy density of 800 Wh kg^{-1}, based on the mass of SWCNT, Figure 2a) at a current density of 1 A g^{-1}, where three distinguished discharge plateaus at 1.8 V, 1.4 V and 0.7 V were shown. It is worth noting that the discharge capacity at 0.7 V can be quite large (more than 1000 mAh g^{-1}, Figure S3), however, a cut-off

voltage was set as 0.72 V to obtain a high discharge voltage region mainly. Compared with the similar tube structure-based MWCNT, the SWCNT shows much higher discharge capacity, especially high-voltage capacity (90 mAh g^{-1} at 1.75 V) while the MWCNT only shows an unobvious discharge plateau at 1.3 V (Figure 2a). It may be explained by the different nanostructure of MNCNT and SWCNT, where the large ion group of $AlCl_4^-$ can be inserted into the interstitial sites of close-packed bundles between SWCNTs while it is hard to be intercalated into the thick-wall MWCNTs. Besides, the larger discharge plateau capacity at 1.2 V can be attributed to the abundant interstitial sites on, inside and between single SWCNTs of bundles. It is also worth mentioning that lots of cathode materials show declined capacity during cycles. For example, MnO_2/Al cell shows a seriously declined discharge capacity due to the collapse of lattice during cycles (Figure 2a), however, the SWCNT cathode shows an enhanced-discharge-capacity phenomenon after a certain cycles' activation, especially for the discharge plateau at 1.2 V, indicating that an interesting intercalation mechanism occurs in the water-in-salt electrolyte system.

The battery also shows good performance at different current densities (From 0.25A g^{-1} to 10A g^{-1}, Figure 2b-d), where enhanced capacity was found after cycling activation. Interestingly, a higher capacity at high voltage plateau of 1.8V was obtained at higher current density instead of decreasing, and a similar phenomenon was reported for large anion (de-)intercalation previously[1, 18], indicating that higher current density can crossover the diffusion barrier easier and thus cause more (de-)intercalation of $AlCl_4^-$ anions. Meanwhile, the discharge plateau at 1.2V was enhanced at a lower current density, indicating a better diffusion process for Al^{3+} cation (de-)intercalation. A fast charge test, that is, charge at a high current density of 10 A g^{-1} and discharge at a low current density of 1A g^{-1}, was conducted, where the cell shows an enhanced high plateau capacity at 1.8V due to the in-depth intercalation of anions during the charging process, indicating the importance of charging condition for anion intercalation. The SWCNT cathode also has good cyclability, which shows almost no decline after 200 cycles at 1A g^{-1} (Figure S4). In addition, a long-term cyclability was shown at a high current density of 5A g^{-1} (Figure 2e), where a higher capacity of 790 mAh g^{-1} and a higher energy density of 980 Wh kg^{-1} were obtained after full activation (Figure S5). Although the discharge capacity slightly decreased after 900 cycles. the discharge capacity would run at a slightly lower level consistently (Figure S6). The degradation can be attributed to two main factors: the SWCNT cathode, which may show fewer intercalation sites by long-term cycles, and the water-in-salt electrolyte system, of

which the ion concentration and the ion diffusion condition may change during cycles. Overall, compared with metal oxides[19] or sulphides [20], the carbon-based materials shows great stability. Thus, different from the previously reported cation-based ion battery, the multi-ion based SWCNT/Al battery shows a high output in the long-term cycles, which surpasses most of the Al-ion batteries and aqueous Zn-ion batteries[21-25], making it a low-cost and high-efficiency solution for large-scale energy storage.

2.3 Triple-ion interaction chemistry of SWCNT cathode in WIS-$AlCl_3$ electrolyte

Different from widely used ionic liquid Al salt electrolyte, complicated intercalation mechanism was shown in aqueous Al-ion battery due to multiple active electrochemical species, such as $AlCl_4^-$, Al^{3+}, H^+ and Cl^-. To reveal the intercalation chemistry in aqueous electrolytes, especially in water-in-salt state electrolytes, a series of comparative experiments utilizing various kinds of electrolytes, such as WIS-$AlCl_3$, WIS-$Al(NO_3)_3$ and WIS-$Al(NO_3)_3$ with HCl additive (WIS-$Al(NO_3)_3$/Cl, see Experimental Methods), were conducted with electrochemical tests and characterization methods, including X-ray powder diffraction (XRD), Raman, FTIR, X-ray photoelectron spectroscopy (XPS) and electrochemical quartz crystal microbalance (EQCM) tests.

An electrochemical dynamics analysis was shown for an overall (de-)intercalation behaviour of SWCNT cathode, where four reduction peaks were found with scan rate gradually increased from 1mV/s to 10mV/s (Figure 3a). Generally, an approach for analysing the electrochemical kinetics process can be described as below:

$$i=av^b,$$

where a and b are adjustable parameters, i is the current, and v is the scan rate. The coefficient b normally varies in the range of 0.5-1.0 where a value of 0.5 represents a diffusion-limited process, while 1.0 indicates a capacitive behaviour.

It is shown that all the intercalation/de-intercalation processes were controlled by both diffusion and capacitive effect (Figure 3b), however, the four reduction peaks did show different characters. Among these reduction peaks, reduction peaks at 1.0V (b=0.53 from figure S7), 0.5V (b=0.73) and -0.1V (b=0.58) vs Ag/AgCl shows less capacitive effect, indicating the possible reactions of (de-)intercalation of $AlCl_4^-$ or Al^{3+}, while the reduction peak at 0.15V (b=0.90) shows more capacitive property, suggesting an adsorption process or a

different insertion type. The properties of these reduction peaks are consistent with the discharge behaviours (Figure 3c), where three clear discharge plateaus were found at 1.05V, 0.5V and 0.05V vs Ag/AgCl, while only a sloping region was found from 0.3V to 0.1V vs Ag/AgCl in WIS-$Al(NO_3)_3$ electrolyte. Thus, these different responses suggest various intercalation behaviours in WIS-$AlCl_3$ AAIB, where $AlCl_4^-$ can insert into SWCNT during charge and Al^{3+}/H^+ can intercalate into SWCNT with the assistance of residential Cl^- ions inside SWCNT (Figure 4a). Further investigation was conducted in WIS-$Al(NO_3)_3$ and WIS-$Al(NO_3)_3$/HCl electrolytes to study the intercalation of Al^{3+}.

2.3.1 Intercalation behaviour in $Al(NO_3)_3$: H^+ and Al^{3+} co-intercalation

Two clear reduction peaks are shown in the CV curve of SWCNT in WIS-$Al(NO_3)_3$ electrolyte by 3-electrode system test (Figure 3d), indicating the ion intercalation/adsorption happens around 0.1V and 0.66V vs Ag/AgCl. respectively. The dynamic analysis confirmed the reduction peak at 0.66V a capacitive process (b=0.96, Figure S8) and the reduction peak at 0.1V (b=0.85, Figure S8) both capacitive and diffusion-controlled processes, which are different from that in WIS-$AlCl_3$ electrolyte (Figure 3a and b), indicating the occurrence of a different intercalation type in WIS-$Al(NO_3)_3$ electrolyte.

As NO_3^- is not likely to be inserted into the SWCNT cathode, Al^{3+} may play a dominant role for ion intercalation in WIS-$Al(NO_3)_3$ electrolyte. However, other ions, for example, H^+, may also affect the intercalation process. CV curve of the SWCNT cathode in H_2SO_4 also shows a reduction peak at around 0.5V (Figure S9a). Although the reduction peak shows a high capacitive feature (b=0.76, Figure S9b) as no obvious peak shift was found with increased scan rate, it should be attributed to the intercalation of H^+ (See Figure S10) as a similar pair of redox peaks was found at 0.45 and 0.51V in H_2SO_4 electrolyte, suggesting that H^+ can be reversely inserted/extracted from the SWCNT. However, it is hard to detect the intercalation of H^+ as no evidence of H^+ intercalation was found by the XRD and Raman test (Figure 4b-d). Luckily, the intercalated ion can be in-situ observed by EQCM (Figure 3e), where the type of intercalated ion can be shown by the revised ratio of the charge and mass changed (Q/M, see supplementary table 1 and 2). The adsorption/desorption process of NO_3^- instead of intercalation was also confirmed by the EQCM test (Figure 3e), where the adsorption/desorption processes were recorded with the liner increased/decreased mass during oxidation/reduction scan without evident peaks. Eliminating the effect of

adsorption/desorption of NO_3^-, it is confirmed that the intercalation process in $Al(NO_3)_3$ electrolyte was a mixture of $(Al\ 6H_2O)^{3+}$ and H_3O^+ as the obtained M/Q value between them at reduction peaks of 0.5V, 0.2V and -0.1V (More Al^{3+} was intercalated at -0.1V due to higher Q/M value, supplementary table 1 and 2). The existence of hydrate ions may result from that hydration shell, which is significant for ion transportation in the aqueous system[26]. It is also worth mentioning that the storage of H^+ is greatly affected by the pH value, where the acidic solution (H_2SO_4, HCl, Figure S11) shows a higher capacity of H^+ than that of salt electrolyte ($Al(NO_3)_3$, $AlCl_3$, Figure 3c).

The intercalation of H^+ was further confirmed by the FTIR spectrum (Figure 4e), where the increased intensity of hydrogen bonding of oxygen-containing groups (2360 cm^{-1})[27] and COOH bonds (1732 cm^{-1})[28] was captured after charge/discharge reaction in the acidic solution (H_2SO_4 and HCl), indicating some H^+ was stored by the formation of -OH/COOH bond on the SWCNT. This result was confirmed by the recent report[27]. However, only a relatively weak COOH peak (531 eV) was found in the WIS-$AlCl_3$ or WIS-$Al(NO_3)_3$ electrolytes (Figure 5a), compared with that observed in HCl electrolyte, indicating the intercalation of H^+ was limited in Al salt based electrolytes, especially water-in-salt state electrolytes. Increased C-H peak was also observed in both HCl and WIS-$AlCl_3$ electrolyte (Figure 5a), suggesting some H^+ can directly bond with carbon like other metal ions, such as Li^+, Na^+ and Al^{3+}. The intercalation method of H^+ was further confirmed by the increased -OH/-COOH groups after long-term cycles (Figure S12, C *1s*), compared with that after initial cycles (Figure S13, C *1s*). To be specific, the amount of O inside the SWCNT was calculated precisely (Table S3), confirming its increase after long-term cycles. To further investigate the effect of the oxidation of the SWCNT cathode, a pre-oxidized SWCNT sample treated by HNO_3 was prepared (see Experimental Methods). Compared with pristine SWCNT (Figure 5a), the oxidized SWCNT shows a distinguished COOH group (Figure S14), indicating that oxygenated functionalities were introduced successfully. As revealed in Figure S15, the oxidized SWCNT shows a clear discharge plateau at 0.35 V vs Ag/AgCl in the WIS-$Al(NO_3)_3$ electrolyte within the 3-electrode system, which is still lower than that of 0.5 V vs Ag/AgCl obtained in the WIS-$Al(NO_3)_3$/HCl electrolyte, indicating a different intercalation mechanism from the Cl^- assisted intercalation of Al^{3+}. An electrochemical dynamics analysis was further conducted (Figure S16), where the obtained reduction peak at 0.2 V vs Ag/AgCl (b=0.84) shows more capacitive feature compared with that obtained by the SWCNT in WIS-$AlCl_3$ electrolyte (reduction peak shown at 0.3 V with b=0.73 in Figure 3a), and it also shows promoted reduction potential compared with that obtained by the SWCNT in WIS-$Al(NO_3)_3$

electrolyte (reduction peak shown at 0.1 V with b=0.85 in Figure 3d). Although the reduction process is still a mixture of the intercalation of Al^{3+} and H^+, it is more like the reduction process occurred at 0.3 V in 1M H_2SO_4 (b=0.78, Figure S9), indicating that it may be mainly attributed to the intercalation of H^+. The XPS measurement further revealed the intercalation mechanism that happened on the oxidized SWCNT cathode (Figure S17), where an enhanced COOH bond was found at both surface and the inner layer of the discharged sample, corresponding to the enhanced capacity of H^+ intercalation. However, the Al-O bond was only found on the surface rather than inside the sample due to the oxidation by the ambient air during storage while the Al-C bond was shown inside the discharged sample instead. These findings suggest that the oxidation of SWCNT cathode can greatly affect the intercalation of H^+, however, much less effect is observed on the intercalation of Al^{3+}.

The intercalation of Al^{3+} can be verified by elemental mapping analysis (Figure 3f), the occurrence of Al and Al_2O_3 peaks at discharged states by the XRD (Figure 4c, the existence of Al_2O_3 please see Figure S18) and the peak shown in the XPS, where the increased density of sp3 peak in C *1s* (Figure 5a) and Al-C peak[29] in Al *2p* (Figure 5c) were found after discharging, indicating the intercalated Al^{3+} may bond with C within the SWCNT. To avoid the possible adsorbed Al on the surface of the SWCNT, the XPS chemical state analysis of sputter depth profiling measurement has been conducted. As shown in Table S3, the Al element shows both at the surface and inside the SWCNT in WIS-$Al(NO_3)_3$, confirming the intercalation of Al^{3+}. Furthermore, the intercalation of Al^{3+} and H^+ is assumed not controversial as the intercalation of Al^{3+} and H^+ is not competing for the same intercalation sites. However, it does exist the possibility that the formed -OH/COOH bond affects the intercalation of Al on the SWCNT surface, though it shows no evidence at this stage.

2.3.2 Intercalation behaviour in WIS-$Al(NO_3)_3$/HCl and WIS-$AlCl_3$ electrolytes: Cl-assisted intercalation

SWCNT shows a high discharge plateau at 0.5V vs Ag/AgCl in WIS-$AlCl_3$ electrolyte (Figure 3c), but it only shows a lower plateau at 0.3V vs Ag/AgCl in WIS-$Al(NO_3)_3$ electrolyte. A similar phenomenon is also observed in solution electrolytes (Figure S10), where the intercalation of Al^{3+} shows two reduction peaks at 0.17V and 0.67V in 1M $Al(NO_3)_3$ electrolyte, however, the intercalation peaks were promoted to 0.38V and 0.74V in 1M $AlCl_3$ electrolytes, indicating that a promoted performance can be achieved by the

additive of Cl^-. To show the effect of Cl^- ion in the electrolyte, further investigation was conducted using WIS-Al$(NO_3)_3$ with the HCl additive. As expected, two main reduction peaks occurred at 0.8V and 0.18V in WIS-Al$(NO_3)_3$/HCl electrolyte (Figure 6a), much higher than that in WIS-Al$(NO_3)_3$ electrolyte (Figure 3d). This also resulted in a higher discharge plateau (Figure 3c), and the mixed intercalation processes of capacitive and diffusion-control were found (b=0.85 and 0.81, Figures S19).

To further reveal the mechanism of Cl-assisted intercalation, a Cl^- pre-intercalated SWCNT cathode (Cl-SWCNT, see Experimental Methods) was tested in WIS-Al$(NO_3)_3$, showing a large reduction peak in the range of 0.6V to -0.2V (Figure 6b). The Cl-SWCNT shows an obvious diffusion-controlled process (b=0.42, Figure S20), which is different from SWCNT in WIS-Al$(NO_3)_3$ and WIS-Al$(NO_3)_3$/HCl electrolytes. This suggests enhanced intercalation of Al^{3+} due to the intercalation of Cl^-. An in-situ EQCM experiment was also conducted in a 1M $AlCl_3$ electrolyte (Figure 6c), revealing that a lot of Cl^- (M/Q=6.5e^{-4}) were intercalated into the cathode material, however, not many were extracted during the cycle. This interesting irreversible intercalation behaviour of Cl^- may result from the high stable Cl-graphene like structure[30-31]. The formation of C-Cl bond was confirmed by FTIR spectrum [32-35] (563, 519 and 434 cm^{-1}, Figure 4e) at a charged stage in HCl solution and both charged and discharged stages in WIS-$AlCl_3$ electrolyte, although the Cl-C signals in WIS-$AlCl_3$ were minor due to two reasons: the limited intercalation amount of Cl^- and the formation of Cl-Al bond. Besides, for both SWCNT charged in 1M HCl and Cl-intercalated SWCNT discharged in WIS-Al$(NO_3)_3$, Cl element was found by XPS test (Figure 5d), indicating that some Cl^- was intercalated in SWCNT cathode even after discharge. Previous reports have shown that Cl-doped graphene obtained higher electrochemical performance[36-37], however, the mechanism, especially for metal ion intercalation, is not revealed.

The intercalated ions at -0.05V and 0.2V vs Ag/AgCl were still confirmed to be the mixture of Al^{3+} and H^+ rather than Cl^- by EQCM (Figure 6c), indicating the assisted function of Cl^-. To further reveal the Cl-assisted intercalation behaviour, the SWCNT cathode at charged and discharged stages in WIS-$AlCl_3$ was examined by FTIR test (Figure 4e), where Cl-Al bond signal occurred at 461, 755 and 957 [38-39] cm^{-1}. The peaks show clear peaks at both charged and discharged states in the WIS-$AlCl_3$ electrolyte, while they are not shown in other electrolytes, suggesting the effect of Cl. Moreover, the intensity of the Cl-Al signal was decreased at the charged stage, while it enhanced at the discharged stage, indicating the Cl-Al

bond was formed during the discharging process by Cl-assisted Al^{3+} intercalation rather than the intercalation of $AlCl_4^-$. By elemental mapping analysis, the C, Al, Cl elements can be seen directly in the discharged SWCNT sample (Figure 6d). However, it mainly shows the signals from the surface of the SWCNT, where the intercalation state inside the SWCNT still demands to be studied. Thus, the *ex-situ* XPS chemical state analysis and XPS with sputter depth profiling provides more evidence. Firstly, the inorganic Cl peak was found at 198.3 eV rather than 199.1 eV of $AlCl_4^-$ group in the discharged SWCNT even after Ar^+ etching (Figure S12), confirming that it is the intercalated Cl^- rather than $AlCl_4^-$ intercalated into the SWCNT. Moreover, the metal-halogen (Al-Cl, 75.3eV) peak[40] was shown in the discharged SWCNT in $AlCl_3$ (both surface and inside, Figure S12 and Figure 5c) and the discharged Cl-intercalated SWCNT in $Al(NO_3)_3$ (Figure 5c), while no evidence of that was found in the discharged SWCNT in $Al(NO_3)_3$ (Figure 5c) by XPS test. In addition, the precise atomic ratio examined by the XPS analysis shows that similar ratios of Al: Cl of 4.3: 1 was obtained inside the discharged SWCNT samples after 30 cycles (Table S3). These suggest the Cl^- assisted Al^{3+} intercalation happens during the discharge process.

Moreover, a first-principles density-functional theory (DFT) based study was conducted for Al ion adsorption in graphene model with/without Cl[41], and the result showed that lower adsorption energy was obtained by the graphene with adsorbed Cl (Figure S21), indicating that Cl-SWCNT structure is favoured by Al intercalation. More conditions have been considered as shown in Figure S22, where gradually increased intercalation energies can be obtained by more adsorbed Cl on SWCNT and decreased energies can also be found by more intercalated Al ions on the Cl-adsorbed SWCNT. It is worth mentioning that even 5 Al ions were intercalated with the Cl-adsorbed graphene model, it shows much lower energy than without the Cl (Figure S21), suggesting the important function of Cl for the intercalation of Al. Based on the ratio of Al: Cl inside the cycled SWCNT measured by the XPS with Ar^+ etch, it shows that mostly 4.3 Al ions were intercalated on the Cl-adsorbed SWCNT (Table S3). This revealed the importance of the intercalated Cl for Al^{3+} intercalation even its amount may be not that large. It is also confirmed that resistance, especially double-layer resistance, was greatly lowered by the intercalation of Cl^- (Figure S23), indicating it is easier for Al^{3+} insertion with pre-intercalation of Cl^-. Thus, the enhanced discharge performance, especially the enlarged discharge plateau capacity at 1.2V (Figure 4b), can be explained by this Cl-assisted intercalation of Al^{3+} ions, which is consistent with the increased Cl and Al amount within SWCNT cathode after long-term cycles examined by XPS (see supplementary table 3).

This Cl-assisted intercalation mechanism was similar to the previously reported halogen conversion-intercalation chemistry of aqueous Li-ion battery[42], where Br-Cl was formed instead of C-Cl during intercalation of Cl^-, indicating that halogen energy storage may be common in the aqueous system. For instance, higher performance (higher reduction potential and response current density) was found in WIS-NaCl than that in WIS-$AlNO_3$ electrolyte (Figure S24).

2.3.3 Intercalation behaviour in WIS-$AlCl_3$ electrolyte: $AlCl_4^-$ intercalation

With no Al^{3+} exists, $AlCl_4^-$ is the only active electrochemical species in ionic liquid [EMIm]Cl/$AlCl_3$ based Al-ion battery, providing a high discharge voltage over 1.7V. In the present study, the high reduction peak at 1.75V only appears in the WIS-$AlCl_3$ electrolyte rather than other aqueous Al salt electrolyte, indicating that $AlCl_4^-$ ion group occurs in WIS-$AlCl_3$ electrolyte (confirmed by our previous study[43], see Electrochemical Measurement for details) rather than reported $Al(OTF)_3$ based AAIBs[10]. Although Cl^- tends to form $AlCl_4^-$ ion group with $AlCl_3$, few $AlCl_3$ exist in an aqueous solution as most $AlCl_3$ can be dissociated into Al^{3+} and Cl^- ions. Thus, $AlCl_4^-$ can hardly be formed in an aqueous battery system except in a "water-in-salt" state electrolyte system, where Al^{3+}, Cl^- and $AlCl_3$ can co-exist at the same time. Moreover, the amount of $AlCl_4^-$ was further confirmed as a function of the applied potential, which can be enhanced at high voltage, boosting the intercalation of $AlCl_4^-$ during charging (see Experimental Methods for details). In the previous section, the de-intercalation of $AlCl_4^-$ can be confirmed by the diffusion-controlled process (b=0.53, Figure 3a and b) at 1.0V vs Ag/AgCl, suggesting the process of $AlCl_4^-$ intercalation into carbon layers, where an $AlCl_4$-graphite intercalation compound (GIC) like structure was formed. Firstly, the SWCNT bundles and MWCNTs have been observed morphologically, where the interlayer of SWNCT bundles was enlarged due to the intercalation of large $AlCl_4^-$ anions (Figure S25), which shows almost no change after discharge due to the small size of Al^{3+} (0.68 pm). As a control group, the pristine and cycled MWCNT samples were also observed (Figure S26), where the interlayer space of the walls shows no change due to almost no intercalation of $AlCl_4^-$, corresponding to its discharge profile without high-voltage plateau. A clear peak of $AlCl_xC$ (PDF: 07-0034)[44] was shown at the charged stage of SWCNT as illustrated in the XRD spectra (Figure 4c). The charged SWCNT was further examined by SEM-Mapping (Figure S27), where an atomic ratio of Al: Cl almost equals to 1:4 was found, suggesting the formation of $AlCl_4^-$GIC. A calculated formula with intercalation stage and discharge voltage

came up with previous researchers[45]. Dino et al.[46] further investigated the relationship by Raman spectra, confirming the intercalation of $AlCl_4^-$ by the up-shift of the G peak in Raman spectra at the fully charged stage (Figure 4d). Furthermore, Δw_G =4 cm^{-1}, indicating an intercalation stage>4, which also corresponds to its discharge plateau of 1.75V rather than 2V (intercalation state <2) in ionic liquid-based Al-ion battery. This revealed that the discharge voltage difference of WIS-$AlCl_3$ based and [EMIm]Cl-$AlCl_3$ based AIBs comes from intercalation difference, where a lower intercalation depth may be obtained in AAIB due to potential H_2O decomposition causing slightly insufficient charge. This suggests that the output of AAIBs can be further promoted by enlarged electrochemical stability window.

Since $AlCl_4^-$ ions are as large as 5.28 Å in diameter, they are regarded to be inserted between layers rather than directly attached on the surface of carbon materials, such as graphite and graphene. Although no layer exists in a single unit of SWCNT, the SWCNT bundles provide interstitial sites between SWCNTs for $AlCl_4^-$ insertion as Figure 4a shown. This insertion site is confirmed by the decreased intensity of the RBM peak (I_{RBM}/I_G), representing the aggregation state[47], as the slight infiltration of the SWCNT bundles can be observed after charging in WIS-$AlCl_3$ by Raman spectrum (Figure 4d and Figure S29). This confirmed the $AlCl_4^-$ insertion into the interlayer sites inside the SWCNT bundles rather than on the surface[48]. This suggests that the agglomeration state can be regarded as an important factor for $AlCl_4^-$ intercalation, which is worth further investigation as shown in Figure S30. To further confirm the intercalation of $AlCl_4^-$, *ex-situ* XPS chemical state analysis and XPS with sputter depth profiling have been carried out as an accurate method to determine the element distribution inside the SWCNT cathode as previous studies reported[49-51] (Figure 7). Increased intensity and up-shift of sp3 peak at charged in C 1s spectra indicates the interlayer intercalation. After Ar^+ etching, the inorganic peak at 197.4 eV disappears since it belongs to the adsorbed Cl on the surface, while the Cl-Al peak at 199.1 eV still exists (Figure S28), corresponding to the chemical bond within the $AlCl_4^-$ group. Besides, a precise ratio of Al: Cl of 1: 3.9 inside the charged SWCNT can be calculated (Table S3), which is close to 1:4 of intercalated $AlCl_4^-$. This indicates that the intercalation of the whole ion group of $AlCl_4^-$ rather than the formation of the bond between Cl and Al.

3 Conclusion

A high discharge capacity SWCNT was developed for AAIB, which shows an excellent discharge capacity of 790 mAh g^{-1} (based on the mass of SWCNT) at 5A g^{-1} for more than

1000 cycles, corresponding to a high energy density of 980 Wh kg^{-1}. The SWCNT cathode also shows a good rate performance, which shows almost no decline at high current density, indicating a potential for fast charge. Moreover, the intercalation chemistry that happens in WIS-$AlCl_3$ electrolyte was firstly revealed, e.g., $AlCl_4^-$ intercalation and Cl-assisted Al^{3+} and H^+ co-intercalation, where halogen was found significant for the high performance of AAIB as higher discharge voltage can be obtained by the formation of Al-Cl bond during discharge. The SWCNT/Al AAIB offers a low-cost solution for the high-performance Al-ion battery development through multi-ion intercalation chemistry. With this multi-ion mechanism, other developed materials, such as graphene, Mxenes and inexpensive graphite-based materials, are expected to show high capacity in the AAIB system, boosting the practical applications of AAIB in the near future.

4 Experimental Methods

Preparation of electrodes and Morphology Characterization: The single-walled carbon nanotube (SWCNT) with carboxymethyl cellulose (CMC) was directly bought from OCSiAl and utilized as cathode material without additives of conductive carbon and binder. For comparison, multi-walled carbon nanotube (MWCNT, Aladdin) and α-MnO_2, which was synthesized by a reported method[52], were also used as cathode active material. The α-MnO_2 cathode is comprised of active material, acetylene black (STREM Chemicals) and PVDF (HSV900, Arkema) (8:1:1). To further investigate the effect of the oxidation of the SWCNT cathode, an oxidized SWCNT sample was prepared by immersing in 1M HNO_3 (VWR International) at 90 ℃ overnight, which is a common method to introduce oxygenated functionalities [53]. The cathode material was dropped onto a carbon paper (Toray Paper 060, Toray) substrate, then dried at 80 ℃ for 2 h in air. High purity aluminium foil (99.9%, Aladdin) was used as anode material. The microstructure and chemical probing of the SWCNT, MWCNT cathodes and the aluminium anode was examined by FE-SEM (Hitachi S-4800) analysis equipped with an EDX detector (Oxford Instruments X-Max 80 EDS Detector) and HR-TEM (FEI Tecnai G2) with TEM-EDX (Oxford Instruments X-Max 80T EDS Detector).

Electrochemical Measurements: A mass ratio of 10:1 of $AlCl_3$ $6H_2O$ and deionized water was utilized to form a water-in-salt (WIS) state electrolyte. The existence of $AlCl_4^-$ in the WIS

state electrolyte has been examined by Raman test in our previous study[43], of which the signal of $AlCl_4^-$ can be observed clearly in the cycled water-in-salt electrolyte, although a weak signal of that was obtained at pristine state. This finding suggests that the $AlCl_4^-$ can be formed by the possible $AlCl_3+Cl^-\rightarrow AlCl_4^-$ [54] reaction as the abundant $AlCl_3$ and Cl^- exists in the water-in-salt electrolyte system or $Al_2Cl_7^-+Cl^-\rightarrow AlCl_4^-$ [55] as $Al_2Cl_7^-$ can be present with excess $AlCl_3$ in the electrolyte. Besides, the reaction $Al_2Cl_7^- \rightarrow Al+AlCl_4^-$ [1] that happens on the negative electrode may form $AlCl_4^-$. That is why the discharge plateau at 1.8V occurs after the activation cycles (Figure S5), then the plateau capacity can be stable, indicating an ion balance inside the electrolyte has been formed. Other WIS electrolytes were prepared in a similar method, of which WIS-$Al(NO_3)_3$ with HCl additive was prepared by the 1M HCl solution instead of the deionized water. And Cl-intercalated SWCNT was synthesised by previously charged for 1000mAh g^{-1} in 1M HCl electrolyte. A comprehensive study of the aqueous WIS electrolyte was conducted in our previous paper[43]. To avoid potential corrosion, the AAIBs were assembled with PMMA shells in a 2-electrode system. The batteries were then cycled at various current densities by a battery testing system (CT2001A, Wuhan Land). Based on the previous report[14,56] and our preliminary study on the intercalation of anion group during the charging process, it is hard to find a clear voltage gap to set a cut-off voltage due to the changeable charge voltage plateau. Thus, similar to the reported AAIB[43] and MnO_2/Zn battery[57], the charge capacity was controlled rather than a charge cut-off voltage. It is worth noting that charge capacity was promoted after a certain cycles' activation to show the enhanced capacity of the SWCNT cathode. And the discharge-cut off voltage was set at 0.72V to obtain the high voltage discharge plateaus and avoid the low discharge plateau as possible. For long-term cycling stability tests, the cell using the WIS electrolyte was charged/discharged at a current density of 1,000 mA g^{-1} and 5,000 mA g^{-1}. To test the rate capability of the SWCNT/Al battery, the current densities were varied from 250 to 10,000 mA g^{-1}. And the max discharge capacity is controlled as large as the charge capacity to avoid the insufficient charge. CV curves were tested by an electrochemical workstation (CHI 660, Shanghai Chenhua). The in-situ electrochemical quartz crystal microbalance (EQCM) experiments were conducted by CHI400C (Shanghai Chenhua), where the SWCNT was dropped on a crystal electrode and then tested in 1M $AlCl_3$ or 1M $Al(NO_3)_3$ electrolytes with a Pt wire counter electrode and an Ag/AgCl reference in the 3-electrode system. The electrolytes used for EQCM experiments only show a low viscosity of 2.03 cp and 1.83 cp for 1M $Al(NO_3)_3$ [58] and 1M $AlCl_3$ [59] at room temperature (298 K), respectively. The applicability of EQCM in more viscous systems has been reported in the literatures. For instance, an

electrolyte of 3M $Zn(CF_3SO_3)_2$ with a viscosity of 55 cP[23] was utilized for the EQCM experiment, and its validity was carefully examined, where the contribution from the viscoelastic effect was confirmed negligible as the full width at half maximum (FWHM) of the tested signal was stable during the test, suggesting that the main contribution can be attributed to the gravimetric change of the electrode[60]. A stable state without the influence of the electrolyte viscosity can be obtained as Figure S27 shown as no mass change was observed after 200 s at the beginning of the test, which further suggests the reliability of the EQCM experiments in dilute aluminium salt electrolyte systems. However, EQCM-D is desired in the future studies for more accurate results including any possible dispersion effects.

XRD, Raman, FTIR and XPS characterization: Avoid the signal interference from carbon paper substrate, the SWCNT samples were prepared by a conductive glass substrate. For the *ex-situ* X-ray diffraction (XRD, Rigaku SmartLab 9kW) study, the SWCNT/Al batteries were charged/discharged at a constant current density of 1 A g^{-1}. To observe the change of peaks in the X-ray diffraction patterns at different stages, SWCNT cathode samples were charged for 800 mAh g^{-1} and discharged to 1.4 and 0.72 V in WIS-$AlCl_3$ electrolyte to obtain samples at fully charged, partially discharged and fully discharged stages. Then, the cathode material was dispersed in D.I water and ethanol solution and centrifugated 5 times to avoid the effect of the attached electrolyte. The SWCNT cathodes were also prepared for Raman, FTIR and X-ray photoelectron spectroscopy (XPS) analysis by the same preparation procedures but in a series of WIS electrolytes. Raman spectra were collected on a Renishaw InVia Raman spectrometer with diode-pumped solid-state (DPSS) laser of 50 mW at 532 nm. The Raman spectrometer was calibrated with Silica standard which is within 520-521 cm^{-1} before the test, and it has the spectra resolution of 0.3 cm^{-1} (FWHM). FTIR spectra were collected on a Bruker Tensor 27 FTIR spectrometer (Hammer Trading Co,.Ltd.) with the resolution of 1 cm^{-1}. XPS spectra were collected on a Thermo Scientific™ K-Alpha™+ spectrometer equipped with a monochromatic Al Kα X-ray source (1486.6 eV) operating at 100 W. Samples were analysed under vacuum ($P < 10^{-8}$ mbar) with a pass energy of 150 eV (survey scans) or 25eV (high-resolution scans). All peaks were calibrated with C1s peak binding energy at 284.8 eV for adventitious carbon. The experimental peaks were fitted with Avantage software. The existence of Al_2O_3 (in XRD[44], Figure 4c, and in XPS [1, 3, 61], Figure 5c) can be attributed to the oxidation of some intercalated Al before measurement. This is firstly confirmed by the XPS depth profile analysis (Figure S13) in this study as the Al-O bond decreased greatly inside the SWCNT sample.

Ex-situ Raman tests on the speciation of $AlCl_4^-$ as a function of potential:

The water-in-salt electrolyte samples have been prepared to show the speciation inside as a function of the applied potential, where the samples were charged/discharged at a series of constant voltages from 0.6 to 2.0 V for 1 h for 1-cycle and 10-cycle. Another two samples cycled for 50 and 150 cycles were also collected to show the effect of the cycle number. As multiple species exist in the water-in-salt electrolytes, it makes the Raman signal more complicated (Figure S31). To be specific, the $Al^{3+}(H_2O)_6$ shows peaks at around 430 and 530 cm^{-1} [62] and the $Al_2Cl_7^-$ shows a strong peak at 300 cm^{-1} [63], indicating its high content. Moreover, different from most reported ionic-liquid based electrolytes for non-aqueous electrolytes, where a clear peak at 345 cm^{-1} occurs, representing the $AlCl_4^-$, this peak in the water-in-salt electrolyte is weak although it would be strengthened after cycles (Figure S31 c and d), indicating the accumulated $AlCl_4^-$ during cycles. These features indicate that the $Al_2Cl_7^-$, $Al^{3+}(H_2O)_6$ and $AlCl_4^-$ can co-exist in the water-in-salt electrolyte, where $Al_2Cl_7^-$ is the major species at initial cycles, which can be transferred to $AlCl_4^-$, making it a complicated system different from the $AlCl_4^-$ dominant ionic liquid electrolytes. Besides, only qualitative analysis can be provided by the analysis of the Raman spectra. Thus, the peaks at 150 and 175 cm^{-1} [63-64] were chosen to show the change of the species, e.g., $Al_2Cl_7^-$ and $AlCl_4^-$ as they are sensitive enough in the water-in-salt system. As shown in Figure S31a, at the first cycle, the $AlCl_4^-$ shows the lowest amount at 0.6 V as the stripping happens at low potential, where the $AlCl_4^-$ was transformed to $Al_2Cl_7^-$, and on the contrary, the plating happens at high potential, where a large amount of $AlCl_4^-$ was found due to the conversion of $Al_2Cl_7^-$ to $AlCl_4^-$. When the applied potential is around 1.2/1.5 V, the changes of $Al_2Cl_7^-$ and $AlCl_4^-$ is not obvious due to the insufficient stripping/plating current. Besides the first cycle, the speciation condition at the 10th cycle has also been tested (Figure S31b), where the amount of $AlCl_4^-$ was found greatly increased at high potential, suggesting speciation balance can be built more efficiently after activation. However, the amount of $AlCl_4^-$ still became low at low potential, indicating the applied potential is important to the speciation inside the electrolyte. Besides, a clear peak at 345 cm^{-1} can be found after long cycles (Figure S31 c and d), indicating the accumulated $AlCl_4^-$. This also indicates that the amount ratio of $AlCl_4^-$ in the water-in-salt electrolyte is much less than that in the ionic liquid, although other species, such as the abundant Al^{3+}, Cl^- and H^+ ions, also play an important role for the battery performance.

Density functional theory (DFT) calculations: DFT calculations were performed using the plane-wave code VASP[65], with valence electrons described by a plane-wave basis with a cutoff energy of 500 eV. Interactions between core and valence electrons were described with the projector augmented wave (PAW) method[66], with $2s^2 2p^2$, $3s^2 3p^1$ and $3s^2 3p^5$ treated as the valence electrons of C, Al and Cl, respectively. The Brillouin zone integrations were performed with the *k*-points sampled using Monkhorst-Pack (MP) grids of $3 \times 3 \times 1$ for a 4×4 graphene supercell, which was used to represent the SWCNT for simplification[41]. The convergence criterion of the electronic self-consistent iteration was set to 10^{-5} eV. The computation used the generalized gradient approximation (GGA) within the Perdew-Burke-Ernzerhof (PBE) parameterization[67]. To model the Cl-assisted intercalation of Al, we first performed a full geometry optimization of graphene and a Cl pre-adsorbed graphene. The Al adsorption was carried out considering all possible adsorption configurations on both surfaces (Figure S21 and S22). The adsorption energies of an Al atom ($E_{\mathrm{Adsorption}}$) were calculated using equation (1):

$$E_{\mathrm{Adsorption}} = E_{\mathrm{Final}} - E_{\mathrm{Al}} - E_{\mathrm{Initial}} \quad (1)$$

where E_{Initial}, E_{Final}, and E_{Al} represent the total energies of the configurations before, after the adsorption of an Al atom, and the energy of a single Al atom, respectively.

The average adsorption energies of per Al atom ($E_{\mathrm{Adsorption}}$) of multi-Al atom were calculated using equation (2):

$$E_{\mathrm{Adsorption}} = (E_{\mathrm{Final}} - \mathrm{n}E_{\mathrm{Al}} - E_{\mathrm{Initial}})/\mathrm{n} \quad (2)$$

where n represents the number of the adsorped Al atoms.

Supporting Information

Supporting Information is available from the Wiley Online Library or from the author.

Acknowledgements

The authors would like to acknowledge the CRCG grant of the University of Hong Kong (201910160008), the National Key R&D Program of China (2018YFB0104400) and the National Natural Science Foundation of China (No. U1864213) for providing funding support to this project. H. W. and Y.Z. would like to thank the UK Engineering and Physical Council (EPSRC) for funding under EP/S000933/1. We also woulk like to thank the University Research Facility in Chemical and Environmental Analysis (UCEA) in the Hong Kong Polytechnic University for the Raman test.

Conflict of Interest

The authors declare no conflict of interest.

Received: ((will be filled in by the editorial staff))
Revised: ((will be filled in by the editorial staff))
Published online: ((will be filled in by the editorial staff))

References:

1. Lin, M.-C.; Gong, M.; Lu, B.; Wu, Y.; Wang, D.-Y.; Guan, M.; Angell, M.; Chen, C.; Yang, J.; Hwang, B.-J.; Dai, H., An ultrafast rechargeable aluminium-ion battery. *Nature* **2015,** *520*, 324.
2. Sun, H.; Wang, W.; Yu, Z.; Yuan, Y.; Wang, S.; Jiao, S., A new aluminium-ion battery with high voltage, high safety and low cost. *Chemical Communications* **2015,** *51* (59), 11892-11895.
3. Song, Y.; Jiao, S.; Tu, J.; Wang, J.; Liu, Y.; Jiao, H.; Mao, X.; Guo, Z.; Fray, D. J., A long-life rechargeable Al ion battery based on molten salts. *Journal of Materials Chemistry A* **2017,** *5* (3), 1282-1291.
4. Das, S. K., Graphene: A Cathode Material of Choice for Aluminum-Ion Batteries. *Angewandte Chemie International Edition* **2018,** *57* (51), 16606-16617.
5. Chen, H.; Xu, H.; Wang, S.; Huang, T.; Xi, J.; Cai, S.; Guo, F.; Xu, Z.; Gao, W.; Gao, C., Ultrafast all-climate aluminum-graphene battery with quarter-million cycle life. *Science Advances* **2017,** *3* (12), eaao7233.
6. Schauerman, C. M.; Ganter, M. J.; Gaustad, G.; Babbitt, C. W.; Raffaelle, R. P.; Landi, B. J., Recycling single-wall carbon nanotube anodes from lithium ion batteries. *Journal of Materials Chemistry* **2012,** *22* (24), 12008-12015.
7. Ziat, Y.; Benyounes, A.; El Rhazouani, O.; Laghlimi, C.; Hammi, M., Single walled carbon nanotubes for enhanced performance of Li-ion batteries. *Turkish Journal of Materials* **2018,** *3* (2), 61-64.
8. Matsushita, T.; Ishii, Y.; Kawasaki, S., Sodium ion battery anode properties of empty and C60-inserted single-walled carbon nanotubes. *Materials Express* **2013,** *3* (1), 30-36.

9. Jiao, H.; Wang, J.; Tu, J.; Lei, H.; Jiao, S., Aluminum - Ion Asymmetric Supercapacitor Incorporating Carbon Nanotubes and an Ionic Liquid Electrolyte: Al/AlCl3 - [EMIm] Cl/CNTs. *Energy Technology* **2016,** *4* (9), 1112-1118.
10. Wu, C.; Gu, S.; Zhang, Q.; Bai, Y.; Li, M.; Yuan, Y.; Wang, H.; Liu, X.; Yuan, Y.; Zhu, N.; Wu, F.; Li, H.; Gu, L.; Lu, J., Electrochemically activated spinel manganese oxide for rechargeable aqueous aluminum battery. *Nature Communications* **2019,** *10* (1), 73.
11. Zhao, Q.; Zachman, M. J.; Al Sadat, W. I.; Zheng, J.; Kourkoutis, L. F.; Archer, L., Solid electrolyte interphases for high-energy aqueous aluminum electrochemical cells. *Science advances* **2018,** *4* (11), eaau8131.
12. Joseph, J.; Nerkar, J.; Tang, C.; Du, A.; O'Mullane, A. P.; Ostrikov, K., Reversible Intercalation of Multivalent Al3+ Ions into Potassium-Rich Cryptomelane Nanowires for Aqueous Rechargeable Al-Ion Batteries. *ChemSusChem* **2019,** *12* (16), 3753-3760.
13. Liu, Y.; Sang, S.; Wu, Q.; Lu, Z.; Liu, K.; Liu, H., The electrochemical behavior of Cl− assisted Al3+ insertion into titanium dioxide nanotube arrays in aqueous solution for aluminum ion batteries. *Electrochimica Acta* **2014,** *143*, 340-346.
14. Sang, S.; Liu, Y.; Zhong, W.; Liu, K.; Liu, H.; Wu, Q., The electrochemical behavior of TiO2-NTAs electrode in H+ and Al3+ coexistent aqueous solution. *Electrochimica Acta* **2016,** *187*, 92-97.
15. Pan, W.; Wang, Y.; Zhang, Y.; Kwok, H. Y. H.; Wu, M.; Zhao, X.; Leung, D. Y. C., A low-cost and dendrite-free rechargeable aluminium-ion battery with superior performance. *Journal of Materials Chemistry A* **2019**.
16. Yu, H.; Jin, Y.; Li, Z.; Peng, F.; Wang, H., Synthesis and characterization of sulfonated single-walled carbon nanotubes and their performance as solid acid catalyst. *Journal of Solid State Chemistry* **2008,** *181* (3), 432-438.
17. Park, O.-K.; Chae, H.-S.; Park, G. Y.; You, N.-H.; Lee, S.; Bang, Y. H.; Hui, D.; Ku, B.-C.; Lee, J. H., Effects of functional group of carbon nanotubes on mechanical properties of carbon fibers. *Composites Part B: Engineering* **2015,** *76*, 159-166.
18. Wu, X.; Xu, Y.; Zhang, C.; Leonard, D. P.; Markir, A.; Lu, J.; Ji, X., Reverse Dual-Ion Battery via a ZnCl2 Water-in-Salt Electrolyte. *Journal of the American Chemical Society* **2019**.
19. Koketsu, T.; Ma, J.; Morgan, B. J.; Body, M.; Legein, C.; Dachraoui, W.; Giannini, M.; Demortière, A.; Salanne, M.; Dardoize, F.; Groult, H.; Borkiewicz, O. J.; Chapman, K. W.; Strasser, P.; Dambournet, D., Reversible magnesium and aluminium ions insertion in cation-deficient anatase TiO2. *Nature Materials* **2017,** *16*, 1142.
20. Yang, W.; Lu, H.; Cao, Y.; Xu, B.; Deng, Y.; Cai, W., Flexible Free-Standing MoS2/Carbon Nanofibers Composite Cathode for Rechargeable Aluminum-Ion Batteries. *ACS Sustainable Chemistry & Engineering* **2019,** *7* (5), 4861-4867.
21. Zhang, N.; Cheng, F.; Liu, J.; Wang, L.; Long, X.; Liu, X.; Li, F.; Chen, J., Rechargeable aqueous zinc-manganese dioxide batteries with high energy and power densities. *Nature communications* **2017,** *8* (1), 405.
22. Xiong, T.; Yu, Z. G.; Wu, H.; Du, Y.; Xie, Q.; Chen, J.; Zhang, Y.-W.; Pennycook, S. J.; Lee, W. S. V.; Xue, J., Defect Engineering of Oxygen-Deficient Manganese Oxide to Achieve High-Performing Aqueous Zinc Ion Battery. *Advanced Energy Materials* **2019,** *9* (14), 1803815.
23. Zhang, N.; Cheng, F.; Liu, Y.; Zhao, Q.; Lei, K.; Chen, C.; Liu, X.; Chen, J., Cation-Deficient Spinel ZnMn2O4 Cathode in Zn(CF3SO3)2 Electrolyte for Rechargeable Aqueous Zn-Ion Battery. *Journal of the American Chemical Society* **2016,** *138* (39), 12894-12901.
24. Li, X.; Xie, X.; Lv, R.; Na, B.; Wang, B.; He, Y., Nanostructured Polypyrrole Composite Aerogels for a Rechargeable Flexible Aqueous Zn-Ion Battery with High Rate Capabilities. *Energy Technology* **2019,** *7* (5), 1801092.

25. Zhang, N.; Dong, Y.; Jia, M.; Bian, X.; Wang, Y.; Qiu, M.; Xu, J.; Liu, Y.; Jiao, L.; Cheng, F., Rechargeable Aqueous Zn–V2O5 Battery with High Energy Density and Long Cycle Life. *ACS Energy Letters* **2018,** *3* (6), 1366-1372.
26. Peng, J.; Cao, D.; He, Z.; Guo, J.; Hapala, P.; Ma, R.; Cheng, B.; Chen, J.; Xie, W. J.; Li, X.-Z.; Jelínek, P.; Xu, L.-M.; Gao, Y. Q.; Wang, E.-G.; Jiang, Y., The effect of hydration number on the interfacial transport of sodium ions. *Nature* **2018,** *557* (7707), 701-705.
27. Shao, H.; Xu, K.; Wu, Y.-C.; Iadecola, A.; Liu, L.; Ma, H.; Qu, L.; Raymundo-Pinero, E.; Zhu, J.; Lin, Z., Unraveling the charge storage mechanism of Ti3C2Tx MXene electrode in acidic electrolyte. *ACS Energy Letters* **2020**.
28. do Amaral Montanheiro, T. L.; Cristóvan, F. H.; Machado, J. P. B.; Tada, D. B.; Durán, N.; Lemes, A. P., Effect of MWCNT functionalization on thermal and electrical properties of PHBV/MWCNT nanocomposites. *Journal of Materials Research* **2015,** *30* (1), 55-65.
29. Xiang, J.; Ding, Y.; Du, L.; Li, J.; Wang, W.; Zhao, C., Growth mechanism of atomic-layer-deposited TiAlC metal gate based on TiCl4 and TMA precursors. *Chinese Physics B* **2016,** *25* (3), 037308.
30. Medeiros, P. V.; Mascarenhas, A. J.; de Brito Mota, F.; de Castilho, C. M., A DFT study of halogen atoms adsorbed on graphene layers. *Nanotechnology* **2010,** *21* (48), 485701.
31. Wang, X.; Sun, G.; Routh, P.; Kim, D.-H.; Huang, W.; Chen, P., Heteroatom-doped graphene materials: syntheses, properties and applications. *Chemical Society Reviews* **2014,** *43* (20), 7067-7098.
32. Zhao, Y., C–Cl Activation by Group IV Metal Oxides in Solid Argon Matrixes: Matrix Isolation Infrared Spectroscopy and Theoretical Investigations of the Reactions of MOx (M = Ti, Zr; x = 1, 2) with CH3Cl. *The Journal of Physical Chemistry A* **2013,** *117* (27), 5664-5674.
33. Tornow, G.; Locht, R.; Kaufel, R.; Baumgärtel, H.; Jochims, H. W., The vacuum ultraviolet photoabsorption and photoelectron spectroscopy of fluorochloroethenes. The 1,1-, cis- and trans-C2H2FCl. *Chemical Physics* **1990,** *146* (1), 115-128.
34. Klapstein, D.; Kuhn, R.; Maier, J. P.; Ochsner, M.; Wyttenbach, T., Spectroscopic characterization of organic cations: emission and laser-excitation spectra of rotationally cooled CH3 C C X+, X Cl, Br. *Chemical Physics* **1986,** *101* (1), 133-146.
35. Darmadi, A.; Haas, A.; Willner, H., Darstellung und Charakterisierung von Selenophosgen/Preparation and Characterization of Selenophosgene. *Zeitschrift für Naturforschung B* **1981,** *36* (10), 1261-1264.
36. Xu, J.; Jeon, I. Y.; Seo, J. M.; Dou, S.; Dai, L.; Baek, J. B., Edge - selectively halogenated graphene nanoplatelets (XGnPs, X= Cl, Br, or I) prepared by ball - milling and used as anode materials for lithium - ion batteries. *Advanced materials* **2014,** *26* (43), 7317-7323.
37. Kou, Z.; Guo, B.; Zhao, Y.; Huang, S.; Meng, T.; Zhang, J.; Li, W.; Amiinu, I. S.; Pu, Z.; Wang, M., Molybdenum carbide-derived chlorine-doped ordered mesoporous carbon with few-layered graphene walls for energy storage applications. *ACS applied materials & interfaces* **2017,** *9* (4), 3702-3712.
38. Hassanzadeh, P.; Citra, A.; Andrews, L.; Neurock, M., Laser-Evaporated Aluminum Atom Reactions with Halogen Molecules. Infrared Spectra of AlXn (X = F, Cl, Br, I; n = 1−3) in Solid Argon. *The Journal of Physical Chemistry* **1996,** *100* (18), 7317-7325.
39. Bahlo, J.; Himmel, H.-J.; Schnöckel, H., Photolytic Reactions of Subvalent Aluminum(I) Halides in the Presence of Dioxygen: Generation and Characterization of the Peroxo Species XAlO2 and XAl(μ-O)2AlX (X = F, Cl, Br) *Inorganic Chemistry* **2002,** *41* (10), 2678-2689.

40. Ramos, R.; Cunge, G.; Pelissier, B.; Joubert, O., Cleaning Aluminum Fluoride coatings from plasma reactor walls in SiCl4/Cl2 plasmas. *Plasma Sources Science and Technology* **2007,** *16*, 711.
41. Huang, C.; Zhang, B.; Luo, Y.; Xiao, D.; Tang, K.; Ruan, Q.; Yang, Y.; Gao, B.; Chu, P. K., A hybrid Co NPs@ CNT nanocomposite as highly efficient electrocatalyst for oxygen evolution reaction. *Applied Surface Science* **2020,** *507*, 145155.
42. Yang, C.; Chen, J.; Ji, X.; Pollard, T. P.; Lü, X.; Sun, C.-J.; Hou, S.; Liu, Q.; Liu, C.; Qing, T.; Wang, Y.; Borodin, O.; Ren, Y.; Xu, K.; Wang, C., Aqueous Li-ion battery enabled by halogen conversion–intercalation chemistry in graphite. *Nature* **2019,** *569* (7755), 245-250.
43. Pan, W.; Wang, Y.; Zhang, Y.; Kwok, H. Y. H.; Wu, M.; Zhao, X.; Leung, D. Y., A low-cost and dendrite-free rechargeable aluminium-ion battery with superior performance. *Journal of Materials Chemistry A* **2019,** *7* (29), 17420-17425.
44. Li, C.; Dong, S.; Tang, R.; Ge, X.; Zhang, Z.; Wang, C.; Lu, Y.; Yin, L., Heteroatomic interface engineering in MOF-derived carbon heterostructures with built-in electric-field effects for high performance Al-ion batteries. *Energy & Environmental Science* **2018,** *11* (11), 3201-3211.
45. Bhauriyal, P.; Mahata, A.; Pathak, B., The staging mechanism of AlCl4 intercalation in a graphite electrode for an aluminium-ion battery. *Physical Chemistry Chemical Physics* **2017,** *19* (11), 7980-7989.
46. Novko, D.; Zhang, Q.; Kaghazchi, P., Nonadiabatic Effects in Raman Spectra of Al Cl 4−-graphite Based Batteries. *Physical Review Applied* **2019,** *12* (2), 024016.
47. Heller, D. A.; Barone, P. W.; Swanson, J. P.; Mayrhofer, R. M.; Strano, M. S., Using Raman Spectroscopy to Elucidate the Aggregation State of Single-Walled Carbon Nanotubes. *The Journal of Physical Chemistry B* **2004,** *108* (22), 6905-6909.
48. Ruch, P. W.; Hardwick, L. J.; Hahn, M.; Foelske, A.; Kötz, R.; Wokaun, A., Electrochemical doping of single-walled carbon nanotubes in double layer capacitors studied by in situ Raman spectroscopy. *Carbon* **2009,** *47* (1), 38-52.
49. Ghidiu, M.; Halim, J.; Kota, S.; Bish, D.; Gogotsi, Y.; Barsoum, M. W., Ion-Exchange and Cation Solvation Reactions in Ti3C2 MXene. *Chemistry of Materials* **2016,** *28* (10), 3507-3514.
50. Miao, X.; Chen, Z.; Wang, N.; Nuli, Y.; Wang, J.; Yang, J.; Hirano, S.-i., Electrospun V2MoO8 as a cathode material for rechargeable batteries with Mg metal anode. *Nano Energy* **2017,** *34*, 26-35.
51. Portenkirchner, E.; Rommel, S.; Szabados, L.; Griesser, C.; Werner, D.; Stock, D.; Kunze - Liebhäuser, J., Sodiation mechanism via reversible surface film formation on metal oxides for sodium - ion batteries. *Nano Select* **2021**.
52. Fan, W.; Liu, F.; Liu, Y.; Wu, Z.; Wang, L.; Zhang, Y.; Huang, Q.; Fu, L.; Wu, Y., A high voltage aqueous zinc–manganese battery using a hybrid alkaline-mild electrolyte. *Chemical Communications* **2020,** *56* (13), 2039-2042.
53. Gao, G.; Pan, M.; Vecitis, C. D., Effect of the oxidation approach on carbon nanotube surface functional groups and electrooxidative filtration performance. *Journal of Materials Chemistry A* **2015,** *3* (14), 7575-7582.
54. Wen, X.; Liu, Y.; Xu, D.; Zhao, Y.; Lake, R. K.; Guo, J., Room-Temperature Electrodeposition of Aluminum via Manipulating Coordination Structure in AlCl3 Solutions. *The journal of physical chemistry letters* **2020,** *11* (4), 1589-1593.
55. Kan, H.-m.; Wang, Z.-w.; Wang, X.-y.; Zhang, N., Electrochemical deposition of aluminum on W electrode from AlCl3-NaCl melts. *Transactions of Nonferrous Metals Society of China* **2010,** *20* (1), 158-164.
56. Wu, X.; Xu, Y.; Zhang, C.; Leonard, D. P.; Markir, A.; Lu, J.; Ji, X., Reverse Dual-Ion Battery via a ZnCl2 Water-in-Salt Electrolyte. *Journal of the American Chemical Society* **2019,** *141* (15), 6338-6344.

57. Chao, D.; Zhou, W.; Ye, C.; Zhang, Q.; Chen, Y.; Gu, L.; Davey, K.; Qiao, S.-Z., An Electrolytic Zn–MnO2 Battery for High-Voltage and Scalable Energy Storage. *Angewandte Chemie International Edition* **2019,** *58* (23), 7823-7828.
58. Zaytsev, I. D.; Aseyev, G. G., *Properties of aqueous solutions of electrolytes*. CRC press: 1992.
59. Maarel, J. R. C. v. d.; Boer, H. R. W. M. d.; Bleijser, J. d.; Bedeaux, D.; Leyte, J. C., On the structure and dynamics of water in AlCl3 solutions from H, D, 17O, and 27Al nuclear magnetic relaxation. *The Journal of Chemical Physics* **1987,** *86* (6), 3373-3379.
60. Zhang, Y.; Liang, Y.; Dong, H.; Wang, X.; Yao, Y., Charge Storage Mechanism of a Quinone Polymer Electrode for Zinc-ion Batteries. *Journal of The Electrochemical Society* **2020,** *167* (7), 070558.
61. Zhang, L.; Chen, L.; Luo, H.; Zhou, X.; Liu, Z., Large-Sized Few-Layer Graphene Enables an Ultrafast and Long-Life Aluminum-Ion Battery. *Advanced Energy Materials* **2017,** *7* (15), 1700034.
62. Stefov, V.; Šoptrajanov, B.; Petruševski, V., Vibrational Spectra of hexaaqua complexes. II. external motions of water molecules in the spectra of AlCl3 ·6H2O. *Journal of molecular structure* **1992,** *267*, 203-208.
63. Yolshina, L.; Shevelin, P.; Druzhinin, K.; Elterman, V.; Yolshina, V.; Muradymov, R., Fast-charged aluminum-ion battery with aluminum-graphene nanocomposite anode. *Ionics* **2021,** *27*.
64. Zhang, Z.; Kitada, A.; Fukami, K.; Yao, Z.; Murase, K., Electrodeposition of an iron thin film with compact and smooth morphology using an ethereal electrolyte. *Electrochimica Acta* **2020,** *348*, 136289.
65. Kresse, G.; Furthmüller, J., Efficiency of ab-initio total energy calculations for metals and semiconductors using a plane-wave basis set. *Computational materials science* **1996,** *6* (1), 15-50.
66. Kresse, G.; Joubert, D., From ultrasoft pseudopotentials to the projector augmented-wave method. *Physical review b* **1999,** *59* (3), 1758.
67. Blöchl, P. E., Projector augmented-wave method. *Physical review B* **1994,** *50* (24), 17953.
68. Theodosiou, A.; Spencer, B. F.; Counsell, J.; Jones, A. N., An XPS/UPS study of the surface/near-surface bonding in nuclear grade graphites: A comparison of monatomic and cluster depth-profiling techniques. *Applied Surface Science* **2020,** *508*, 144764.

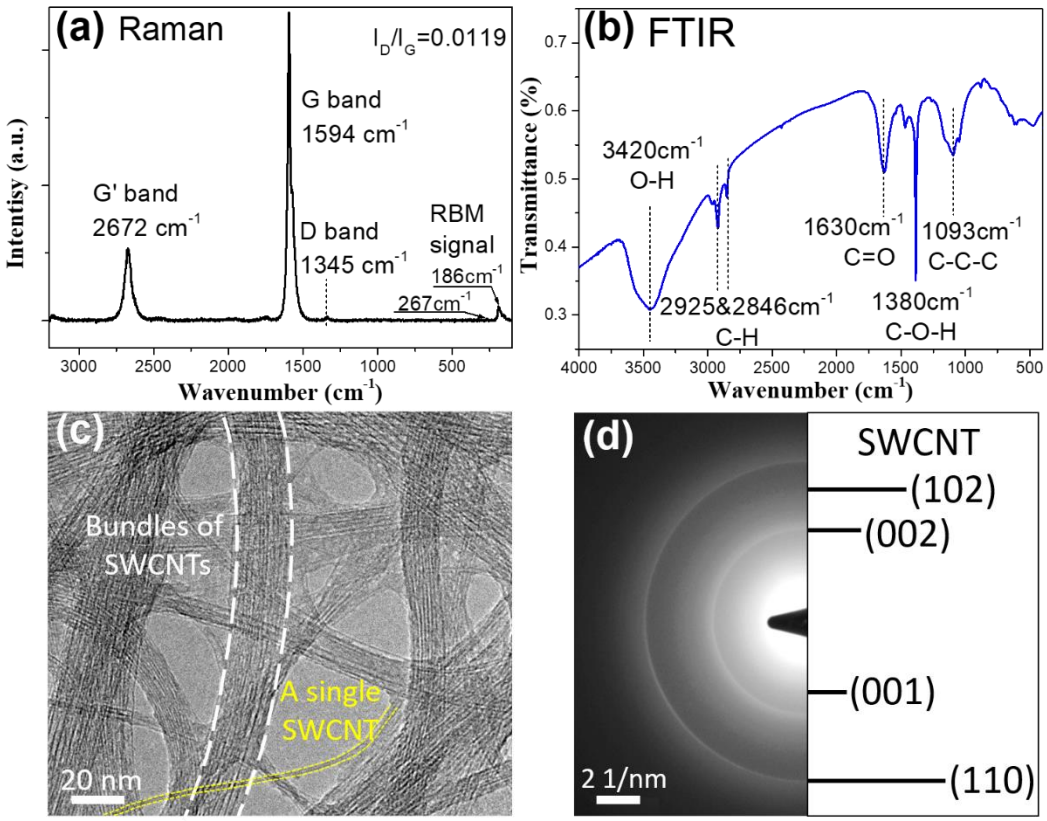

Figure 1. Characterization of single-walled carbon nanotube (SWCNT). a) Raman spectrum, b) FTIR spectrum, c) TEM image and d) SAED figure of SWCNT cathode.

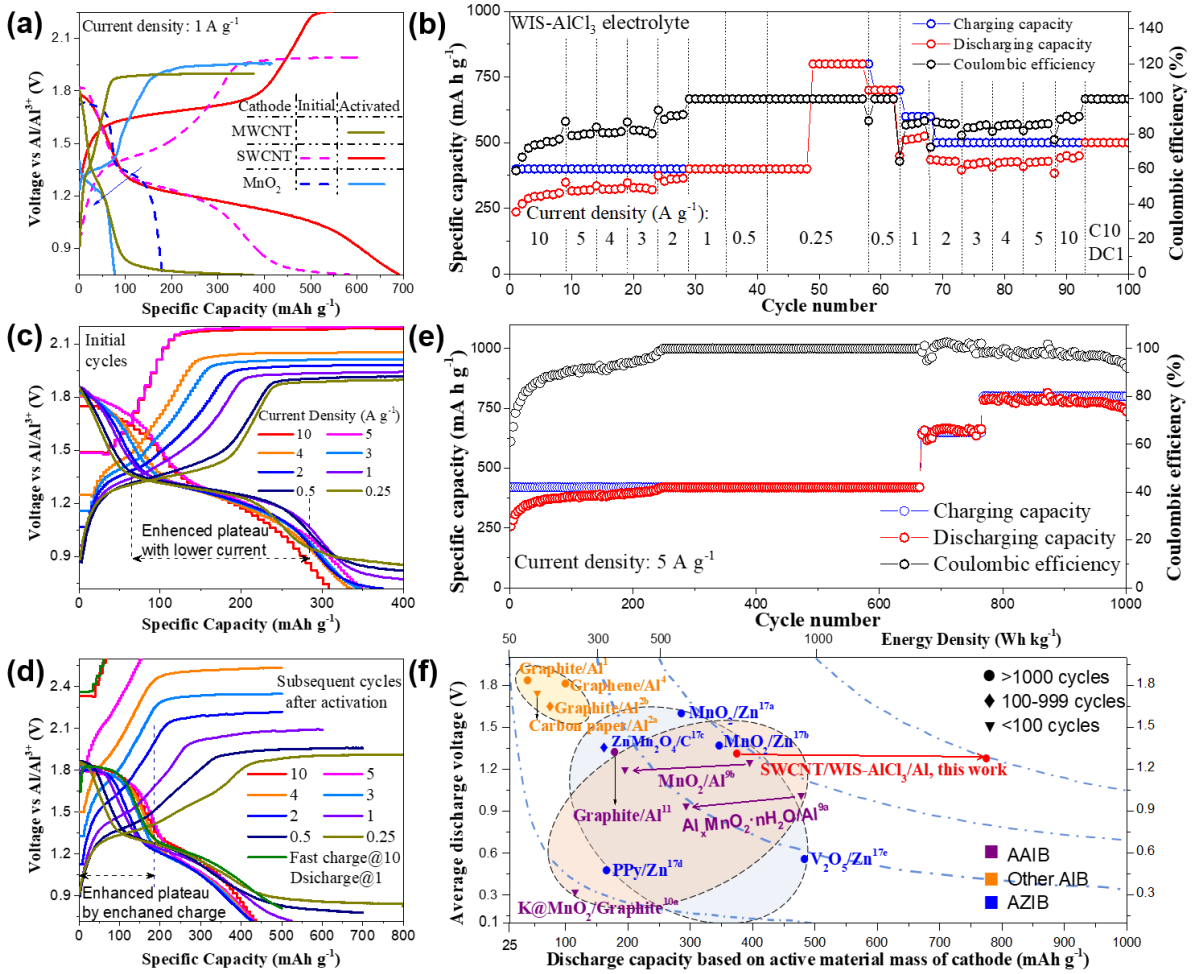

Figure 2. Electrochemical performance of an SWCNT/Al cell. a) Galvanostatic charge and discharge curves of AAIB with cathode material of MWCNT, SWCNT and MnO_2 in WIS-$AlCl_3$ electrolytes. b) Charge/discharge capability and coulombic efficiency at a series of current densities, where charge capacity was increased after 50 cycles for sufficient charge. (c and d) Galvanostatic charge and discharge curves at a series of current densities for initial cycles and subsequent cycles after activation, where enhanced capacity was found after activation. e) Cyclicality for charge/discharge capability and coulombic efficiency at a high current density of 5 A g^{-1}. f). Comparison of electrochemical performance (including average voltage, capacity, energy density and cycle life) for various non-aqueous AIBs, AAIBs and AZIBs.

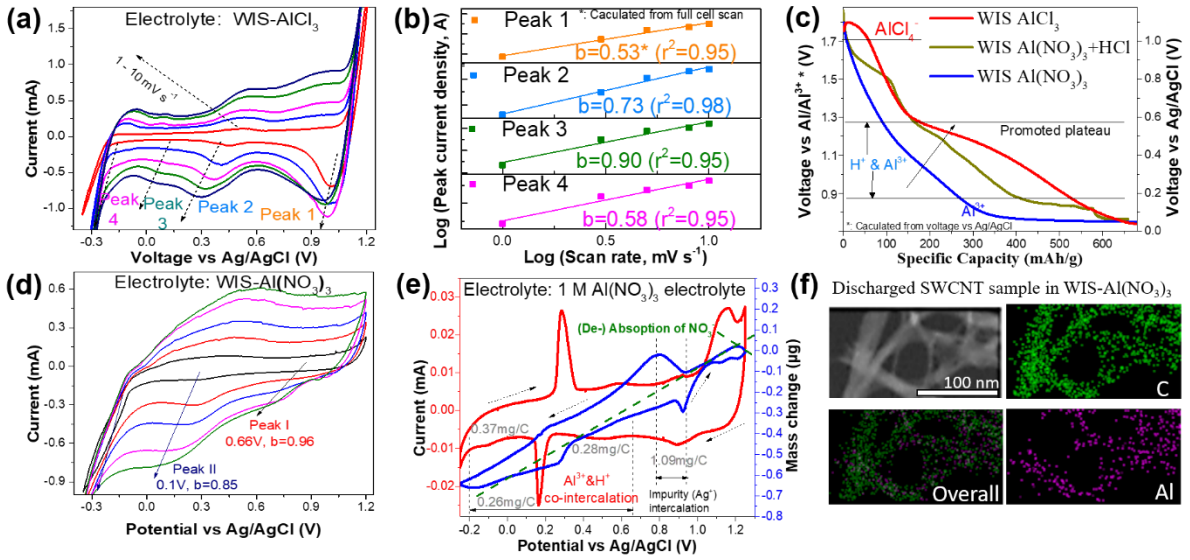

Figure 3. Electrochemical analysis for multi-ion intercalation chemistry. a and b) CV curves at a series of scan rates of SWCNT in WIS-$AlCl_3$ and corresponding linear fitting figure of log (peak current density) and log (scan rate). c) Galvanostatic discharge curves of SWCNT in WIS-$Al(NO_3)_3$, WIS-$Al(NO_3)_3$/HCl and WIS-$AlCl_3$ electrolytes. d) CV curves at a series of scan rates of SWCNT in WIS-$Al(NO_3)_3$ electrolyte. e) In-situ EQCM tests of SWCNT cathode in 1M $Al(NO_3)_3$. f) EDX-mapping of SWCNT at discharged state in WIS-$Al(NO_3)_3$ electrolyte.

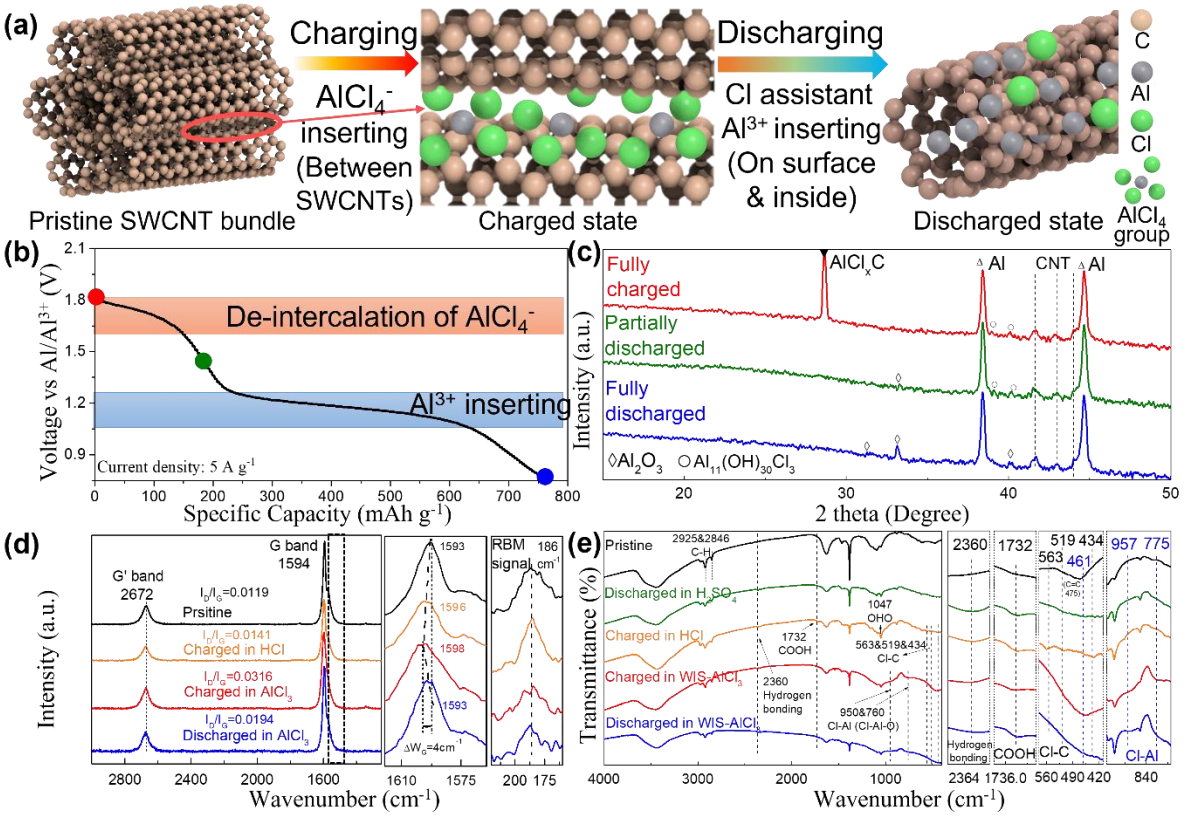

Figure 4. Mechanism of multi-ion intercalation into the SWCNT cathode. a) Schematic diagram of ion intercalation/de-intercalation during charge/discharge process; b) Discharge

profile showing de-intercalation of $AlCl_4^-$ and Al^{3+} insertion stages. c) XRD spectrum ranging from 10-50 degree; d) Raman spectrum ranging from 3000-1000 cm^{-1}, where G band and RBM signals were enlarged. e) FTIR spectrum ranging from 4000-400 cm^{-1}, where some important ranges were enlarged.

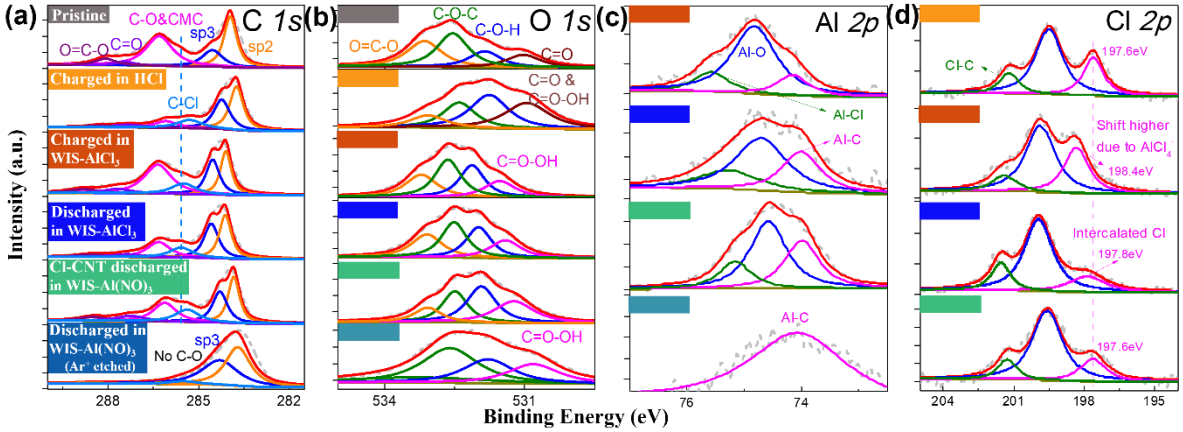

Figure 5. XPS analysis of SWCNT to confirm the intercalation mechanism: XPS data of (a) C 1s, (b) O 1s, (c) Al 2p and (d) Cl 2p of charged and discharged SWCNT cathode in various electrolytes.

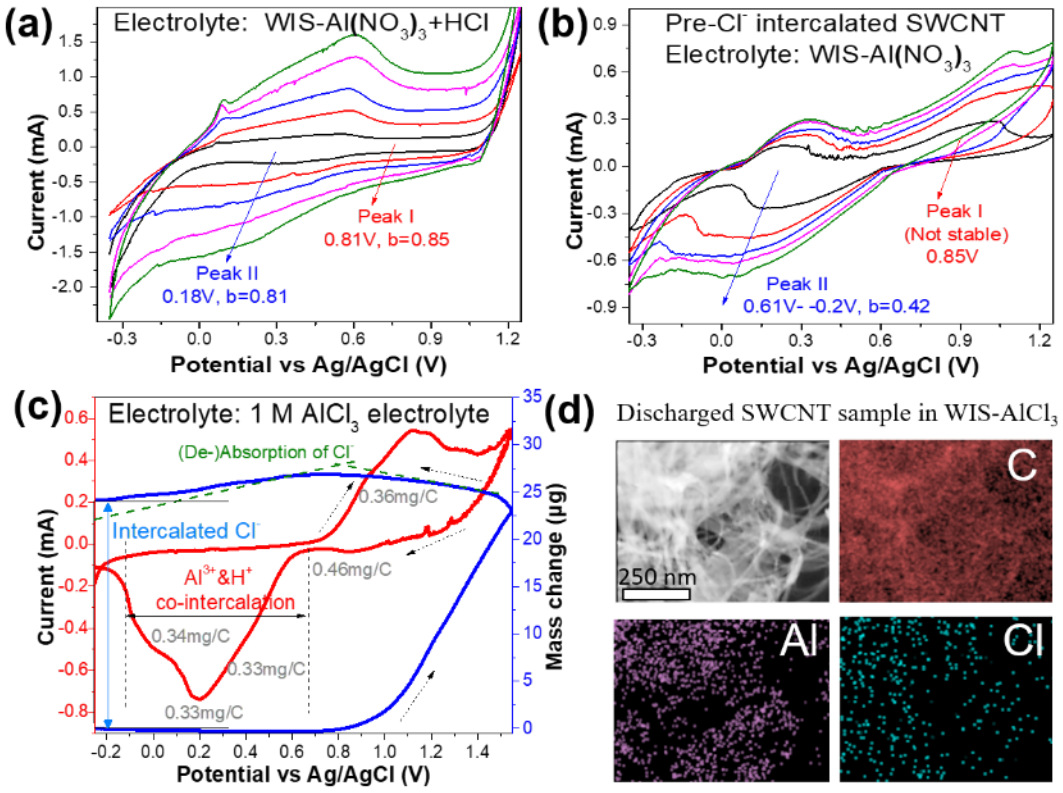

Figure 6. Electrochemical analysis for Cl^- assisted Al^{3+} intercalation mechanism. a) CV curves at a series of scan rates of SWCNT in WIS-$Al(NO_3)_3$/HCl electrolyte and Cl-intercalated SWCNT in $Al(NO_3)_3$ electrolyte. c) In-situ EQCM tests of SWCNT cathode in 1M $AlCl_3$. d) EDX-mapping of SWCNT at discharged state in WIS-$AlCl_3$ electrolyte.

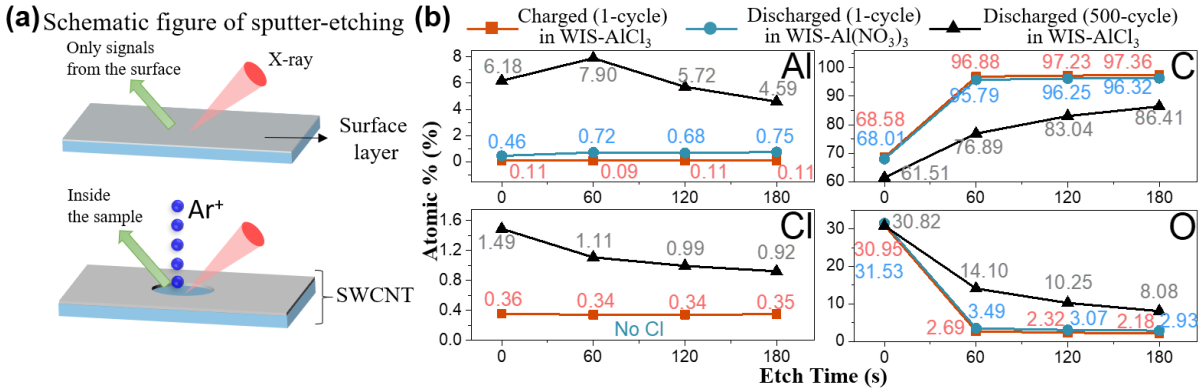

Figure 7. XPS chemical state analysis of sputter depth profiling measurements to show the ion intercalation state inside the SWCNT cathode. a) Schematic figure of the sputter-etching technology, which allows XPS analysis to show the inner state of the sample. b) XPS depth profile of the charged and discharged SWCNT in WIS-AlCl3 and WIS-Al$(NO_3)_3$.

Table of content:

A high-capacity single-walled carbon nanotube was first utilized as the cathode with a "water-in-salt" electrolyte for an aqueous Al-ion battery. It was found that the carbon nanotube cathode exhibits superior energy density, which can be attributed to the multi-ion intercalation mechanism, that is, the high-voltage deintercalation of $AlCl_4^-$ and the high-capacity intercalation of Al^{3+} cation.

High-Energy SWCNT Cathode for Aqueous Al-ion Battery Boosted by Multi-ion Intercalation Chemistry

W. D. Pan, Y. Zhao, J. J. Mao, Y. F. Wang, X. L. Zhao, K. W. Leong, S. J. Luo, X. H. Liu**, H. Z. Wang, J. Xuan, S. C. Yang, Y. Chen, D.Y.C Leung*

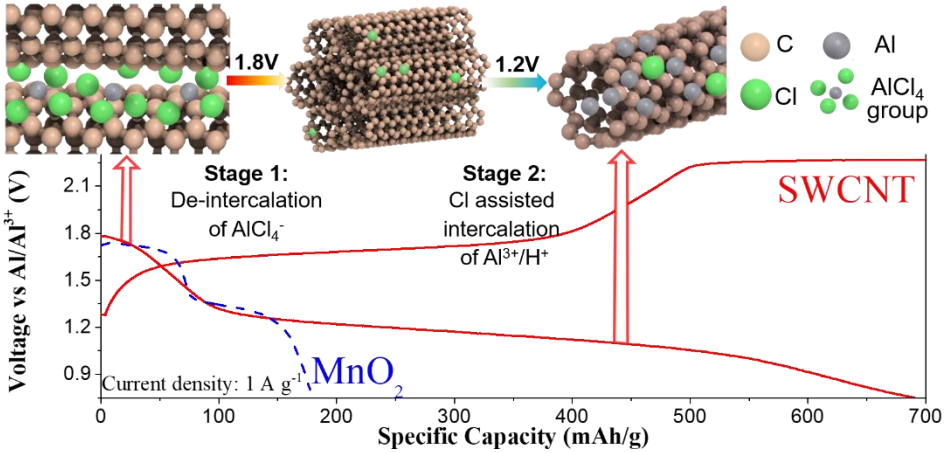

Supporting Information

High-Energy SWCNT Cathode for Aqueous Al-ion Battery Boosted by Multi-ion Intercalation Chemistry

W. D. Pan, Y. Zhao, J. J. Mao, Y. F. Wang, X. L. Zhao, K. W. Leong, S. J. Luo, X. H. Liu**, H. Z. Wang, J. Xuan, S. C. Yang, Y. Chen, D.Y.C Leung*

Table S1 Q/M data of possible ions, where OH^- is not likely to be the main electrochemical active species due to the acidic nature of the electrolytes.

Electrochemical active ions (EAIs)	Q/M (g/C)	Electrochemical active ions (EAIs)	Q/M (g/C)
$AlCl_4^-$	1.73E-03	NO_3^-	6.44E-04
Al^{3+}	9.34E-05	$(Al\ 6H_2O)^{3+}$	4.67E-04
Cl^-	3.68E-04	H_3O^+	1.97E-04
H^+	2.07E-05	OH^-	1.76E-04

Table S2 Q/M data obtained from EQCM test and revised Q/M, of which adsorbed ions were extracted, at non-peak region and reduction/oxidation peak region of the CV curves.

In 1M $AlNO_3$			
Potential region	Original Q/M (g/C)	Revised Q/M (g/C)	Possible ions
1.2-1.1 (Non-peak)	6.5E-04	/	NO_3^- (De-absorption)
0.9-0.8 (Reduction)	4.47E-04	1.09E-03	Ag^+
0.5-0.35 (Reduction)	-3.66E-04	2.78E-04	$(Al\ 6H_2O)^{3+}$ &H_3O^+
0.16-0.14 (Reduction)	-3.82E-04	2.62E-04	
-0.12- -0.175 (Reduction)	-2.69E-04	3.75E-04	

In 1M $AlCl_3$			
Potential region	Original Q/M (g/C)	Revised Q/M (g/C)	Possible ions
1.2-1.0 (Non-peak)	3.62E-04	/	Cl^- (Absorption)
0.8-1.2 (Non-peak)	3.65E-04	/	Cl^- (Intercalation &Absorption)
0.85-0.75 (Reduction)	9.39E-05	4.56E-04	May $AlCl_4^-$ with Cl^-
0.45-0.3 (Reduction)	-3.17E-05	3.30E-04	$(Al\ 6H_2O)^{3+}$ &H_3O^+
0.3-0.1 (Reduction)	-2.99E-05	3.32E-04	
0.1- -0.1 (Reduction)	-1.91E-05	3.43E-04	

In 1M $Al(NO_3)_3$ electrolyte, the absorption/de-absorption of NO_3^- is evident, as mass increased/decreased almost linearity with lost/accumulated charge. However, the Cl^- ion shows standard intercalation behaviour instead of absorption since almost no mass change was observed after the oxidation peak.

Table S3 Atomic ratio of C, Al, Cl, O measured by XPS test after Ar^+ sputtering etch. Data with 95% confidence bounds.

Element (Etching for 60 s)	**Charged in WIS-$AlCl_3$ at 1-cycle**	**Discharged in WIS-$Al(NO_3)_3$ at 1-cycle**	**Discharged in WIS-$AlCl_3$ at 20-cycle**
Al	0.091 ± 0.006 (±6.6%)	0.693 ± 0.064 (±9%)	1.385 ± 0.158 (±11.4%)

Cl	0.351 ± 0.028 (±8.0%)	/	0.320 ± 0.049 (±15.3%)
C	96.757 ± 0.414 (±0.4%)	95.968 ± 0.365 (±0.4%)	92.587 ± 0.877 (±0.9%)
O	2.800 ± 0.404 (±14.4%)	3.341 ± 0.295 (±8.8%)	5.708 ± 0.700 (±12.3%)
Cl: Al	3.857:1	/	1:4.328
Al: C	0.094%	0.722%	1.496%
Calculated formula	$Al_{0.001}Cl_{0.004}O_{0.029}C$	$Al_{0.007}O_{0.035}C$	$Al_{0.015}Cl_{0.003}O_{0.062}C$

Note: The relatively large error (~10%) for Al, Cl and O elements is because that the $AlCl_4^-$, Al^{3+}, Cl^- and H^+ cannot be uniformly intercalated into the SWCNT cathode, causing fluctuation in the measurement.

A Cl: Al ratio of 3.9:1 was obtained inside the charged SWCNT sample, indicating the intercalation of $AlCl_4^-$. This ratio is not exactly 4 because the amount of Al may be affected by the amount of adsorbed Al. Compared with WIS-$Al(NO_3)_3$ electrolyte, a higher amount of intercalated Al was found in WIS-$AlCl_3$ electrolyte, where a high ratio of Al: Cl, i.e. 4.3:1, was obtained inside the discharged SWCNT sample (etched for 60 s), compared with that of 0.26:1 inside the charged SWCNT sample. This indicates the Cl^- assisted intercalation of Al^{3+} during the discharging process, which is different from the intercalation of $AlCl_4^-$ during the charging process

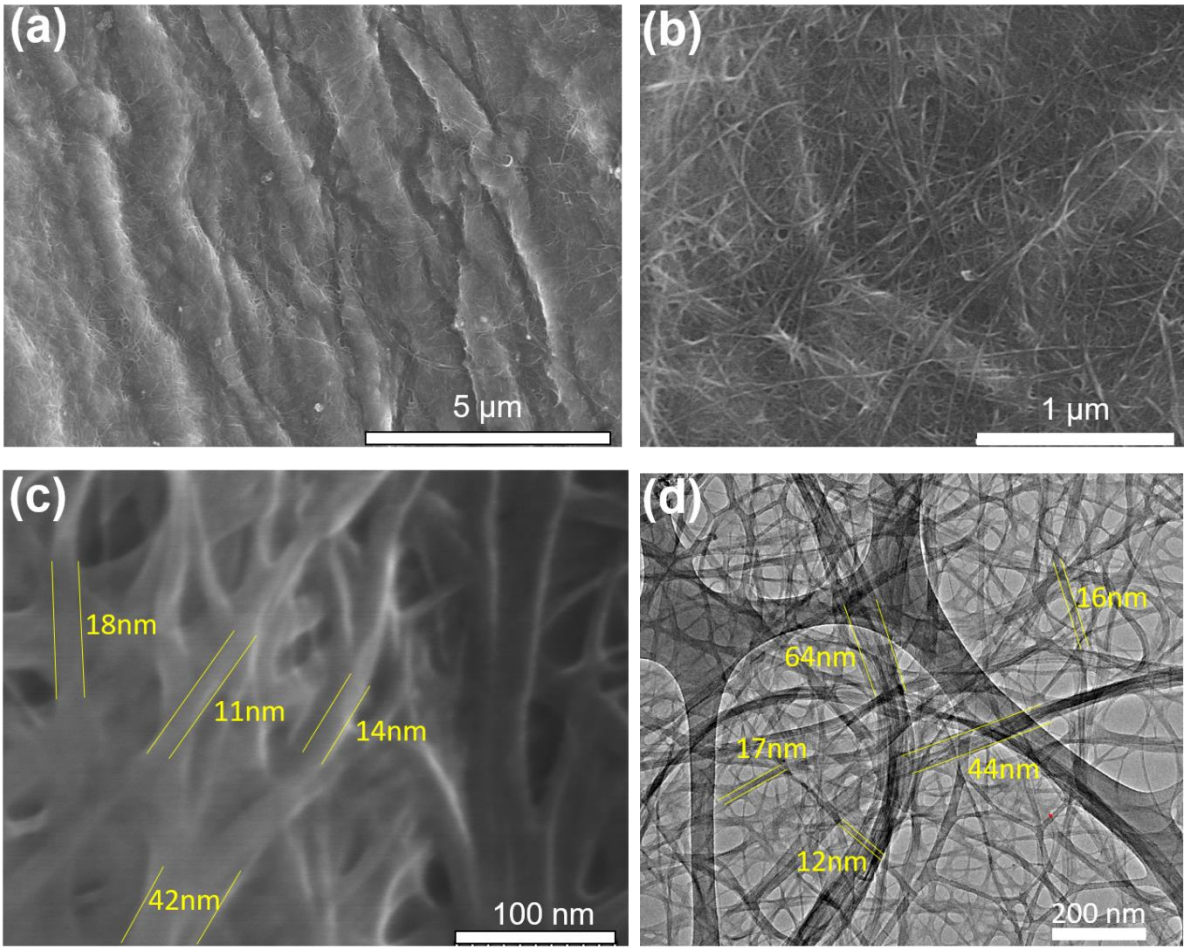

Figure S1 (a-c) SEM and (d) TEM images of SWCNT, where a dense SWCNT cathode layer was observed by SEM and a dispersed SWCNT sample was shown by TEM to see its microstructure. The size of SWCNT bundles was labelled, where they are mostly around 15 nm.

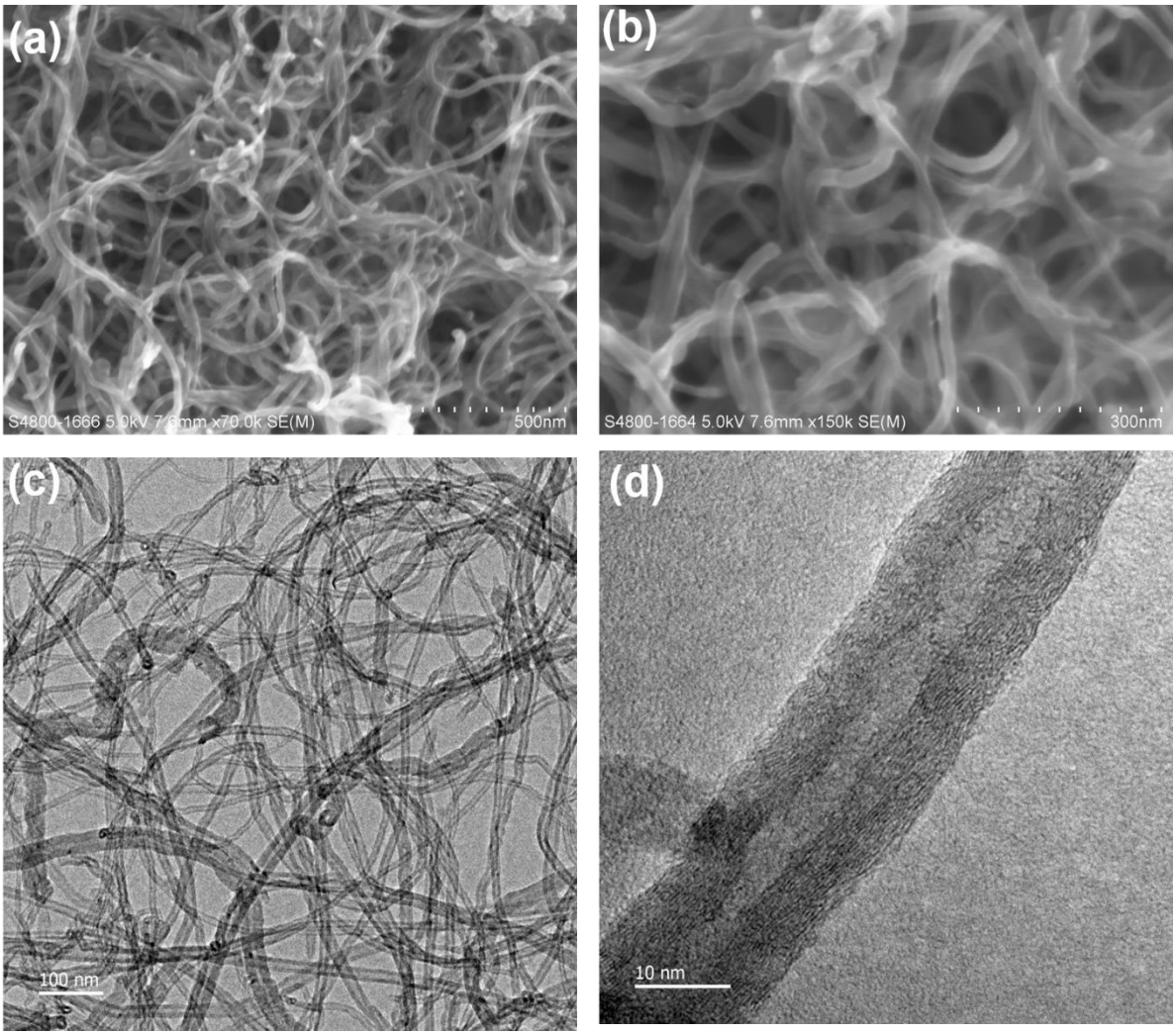

Figure S2 (a and b) SEM and (c and d) TEM images of MWCNT, where a thick wall (close to 10nm) can be found.

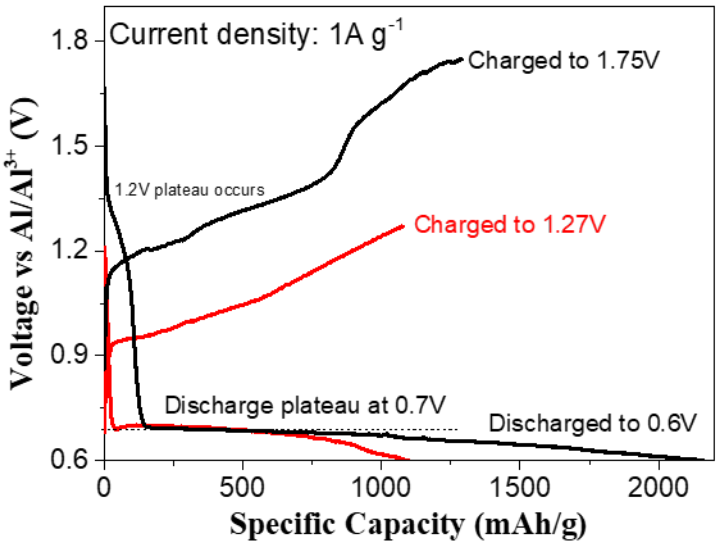

Figure S3 Galvanostatic charge and discharge curves at low discharge plateau region at a current density of 5 A g^{-1}. When the SWCNT/Al cell was charged to 1.27V, only a low voltage discharge plateau at 0.7V was shown, while a higher voltage discharge plateau at

1.2V was displayed by charging to 1.75V, indicating both the discharge voltage plateaus at 1.2V and 0.7V related to ion intercalation.

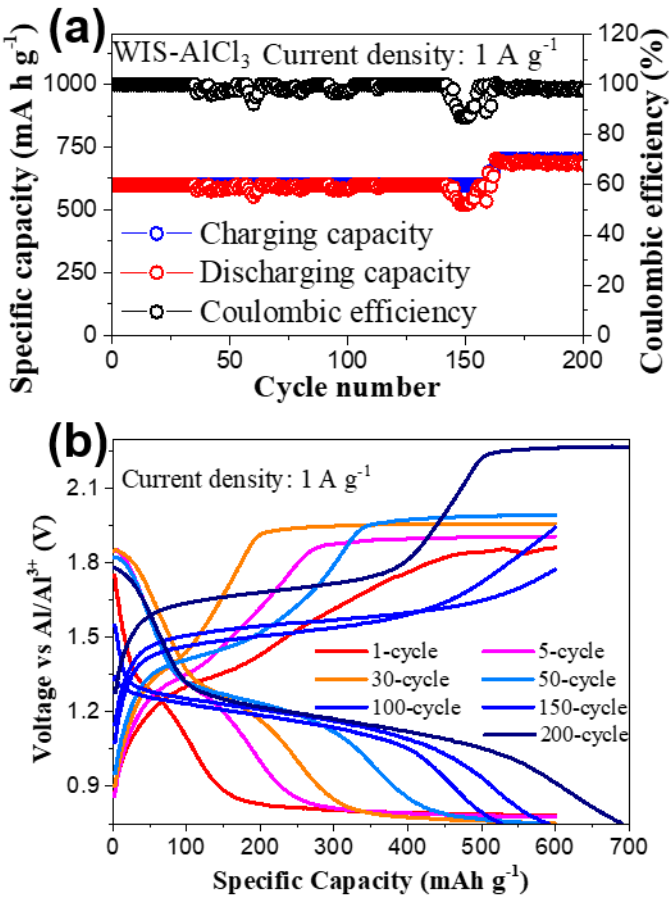

Figure S4 a) Cyclicality for charge/discharge capability and coulombic efficiency at a current density of 1 A g^{-1} and corresponding b) Galvanostatic charge and discharge curves at different cycles. It is worth noting that charge/discharge capacity was limited by 600 mA g^{-1} rather than a voltage-cut off to avoid overcharge/overdischarge. No high voltage plateau was shown at the first cycle, indicating limited $AlCl_4^-$ ions inside the electrolyte. Then, both the discharge plateaus at 1.8V and 1.2V were enlarged until the discharge plateau at 1.2V plays a dominant role due to the insufficient charge. Finally, an enhanced capacity with two plateaus was obtained by increased charging capacity.

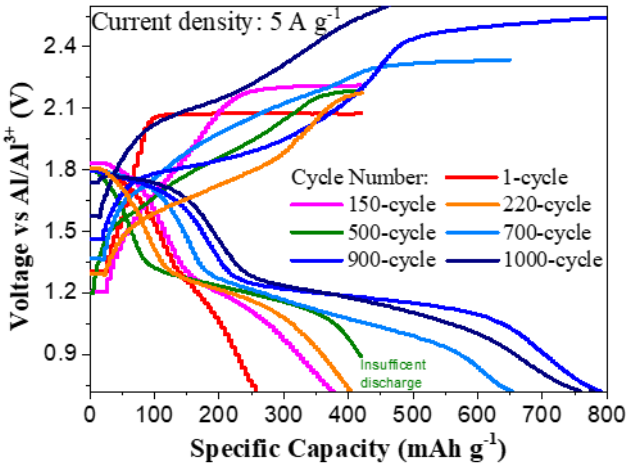

Figure S5 Galvanostatic charge and discharge curves at different cycles at a current density of 5 A g^{-1}. At initial cycles, both the discharge plateaus at 1.8V and 1.2V were enlarged, indicating an optimized electrolyte component was formed. Subsequently, the discharge plateau at 1.2V continued to be enlarged while the plateau capacity at 1.8V decreases, showing enhanced intercalation of Al while the $AlCl_4^-$ intercalation was decreased at the same time due to insufficient charge. Finally, an enhanced capacity with two plateaus was obtained by increased charging capacity.

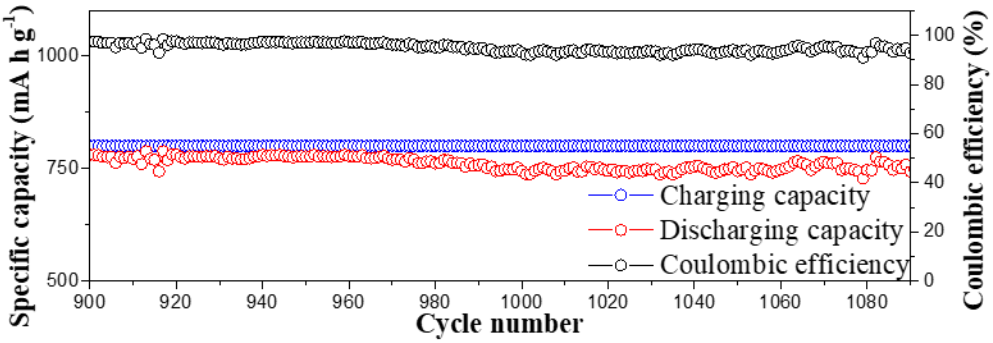

Figure S6 Charge/discharge capabilities and coulombic efficiencies for 900-1090 cycles at a current density of 1 A g^{-1} to show the battery performance degradation process after 900 cycles.

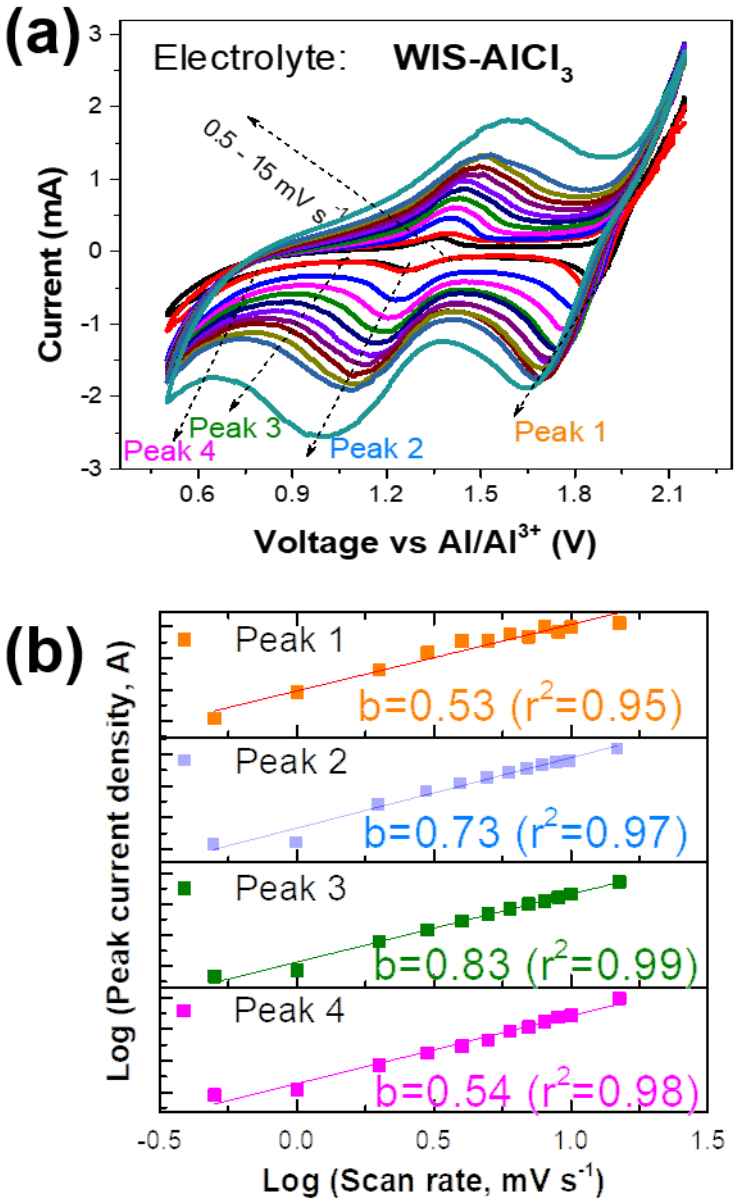

Figure S7 a) Cyclic voltammetry (CV) of the cycled SWCNT/Al cell at a series of scan rates in WIS-$AlCl_3$ electrolyte and corresponding b) Linear fitting of log (peak current density) and log (scan rate). The peak 2 at 1.2V was enhanced compared with that of initial cycles and the peak 3 and 4 became less obvious.

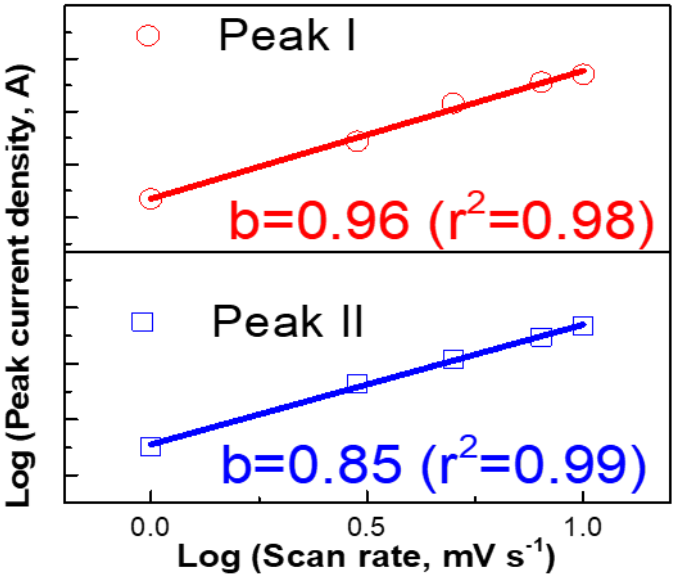

Figure S8 Linear fitting of log (peak current density) and log (scan rate) of the CV curves of SWCNT in WIS-$Al(NO_3)_3$ electrolyte. Peak I displays a capacitive feature, and peak II shows both diffusion-controlled and capacitive properties, indicating different types of intercalation.

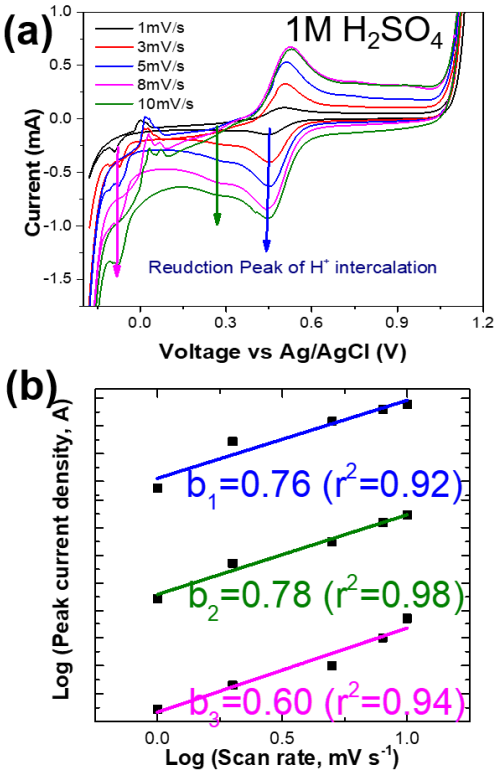

Figure S9 (a) Cyclic voltammetry (CV) of the SWCNT in 1M H_2SO_4 at a series of scan rates by 3-electrode system and corresponding (b) Linear fitting of log (peak current density) and log (scan rate).

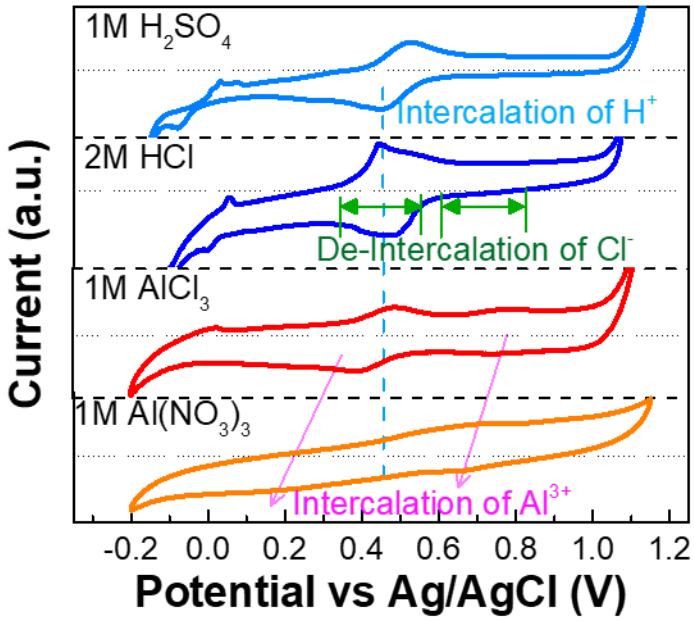

Figure S10 Cyclic voltammetry (CV) of the SWCNT in 1M H_2SO_4, 2M HCl, 1M $AlCl_3$ and 1M $Al(NO_3)_3$ electrolytes by the 3-electrode system. Among these CV curves, the intercalation peak of H^+ intercalations shows around 0.5V, although it is limited in Al-based electrolytes.

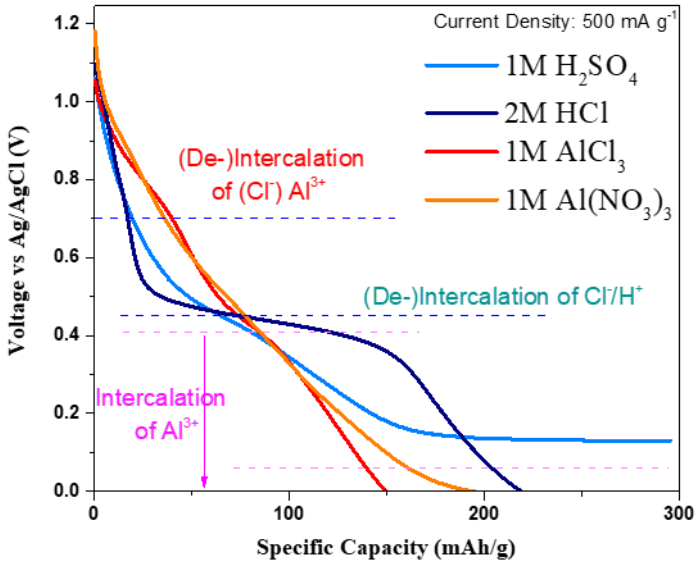

Figure S11 Galvanostatic discharge curves of SWCNT in 1M H_2SO_4, 2M HCl, 1M $AlCl_3$ and 1M $Al(NO_3)_3$ electrolytes by the 3-electrode system at a current density of 500 mA g^{-1}. An obvious discharge plateau was found in 1M H_2SO_4 and 2M HCl electrolytes due to the intercalation of H^+, however, only a sloping region was found in 1M $AlCl_3$ and 1M $Al(NO_3)_3$ electrolytes, indicating the limited concentration of both Al^{3+} and H^+ affects the discharge behaviour.

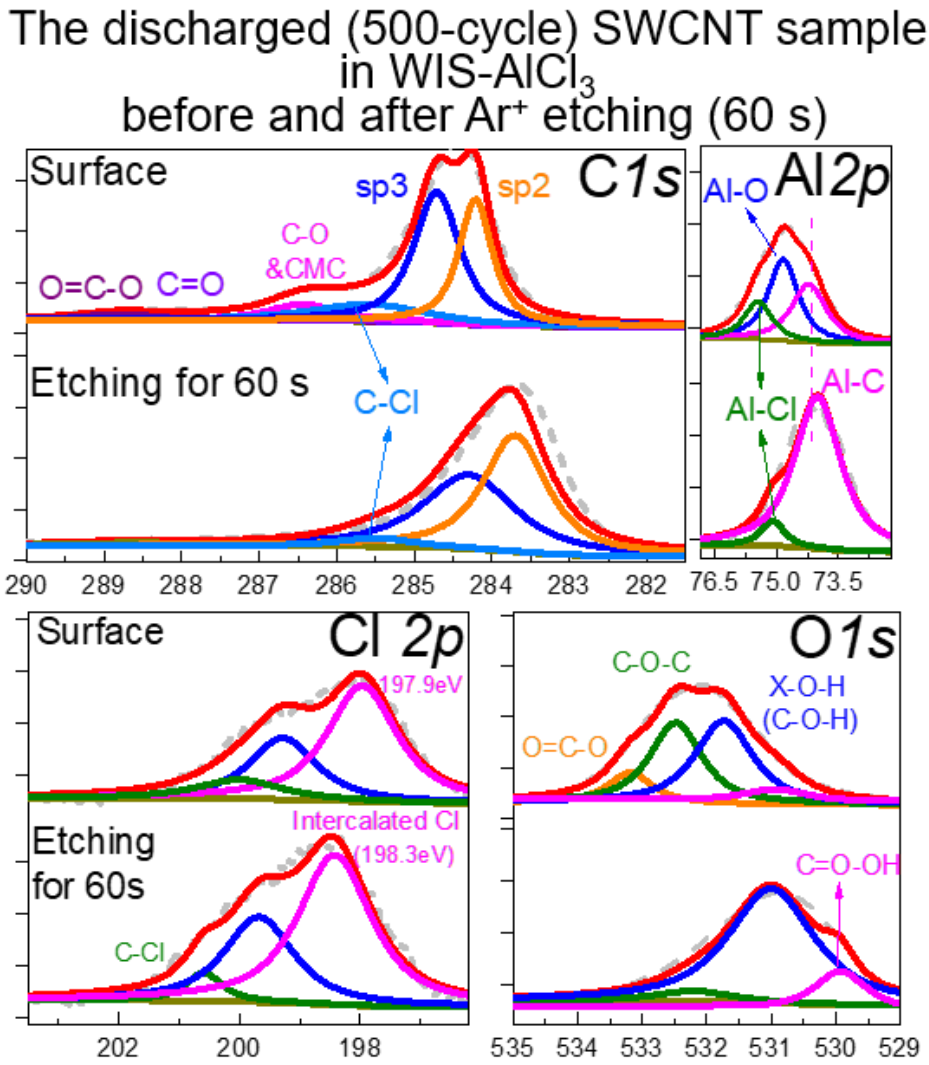

Figure S12 XPS depth profile analysis of C 1s, Al 2p, O 1s and Cl 2p of discharged SWCNT (500-cycle) in WIS-$AlCl_3$ electrolyte, which was collected at pristine and after etching for 60 s, corresponding to a depth of 7 nm approximately[68].

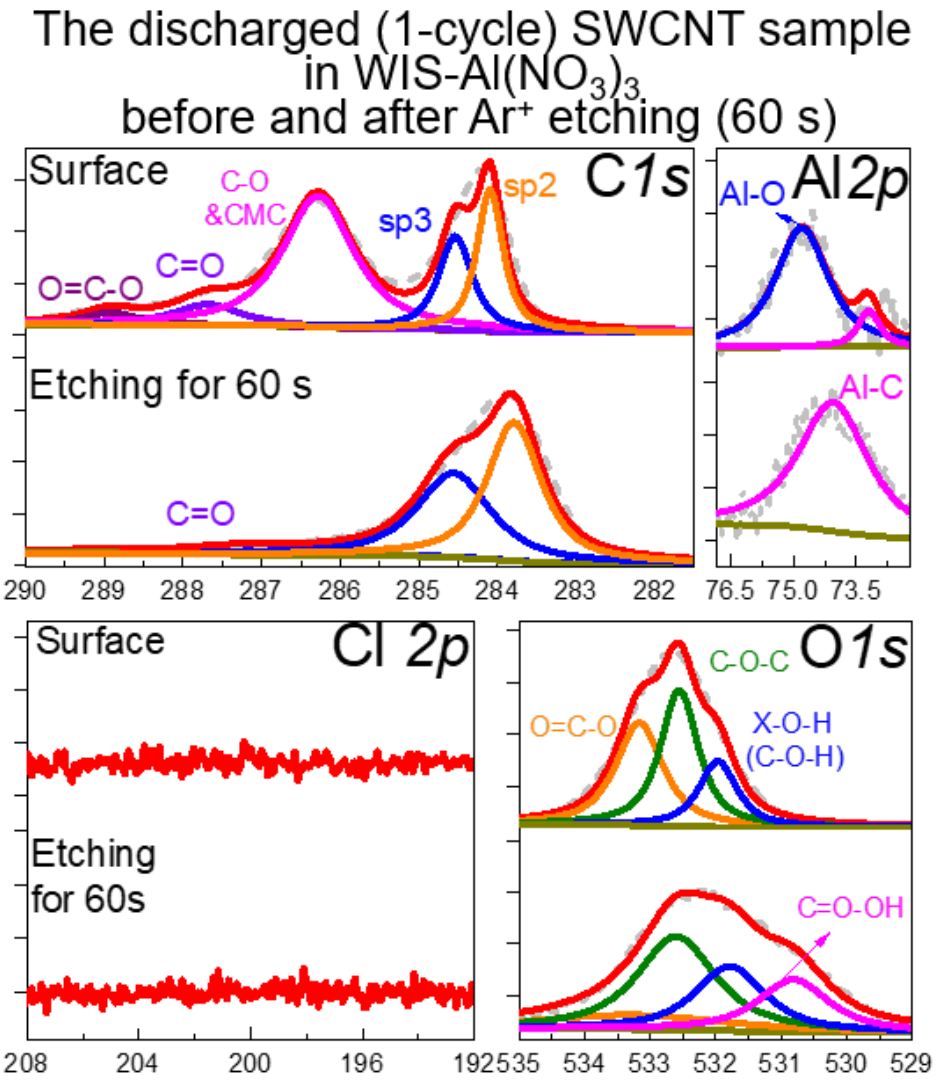

Figure S13 XPS depth profile analysis of C 1s, Al 2p, O 1s and Cl 2p of discharged SWCNT (1-cycle) in WIS-Al$(NO_3)_3$ electrolyte, which was collected at pristine and after etching for 60 s.

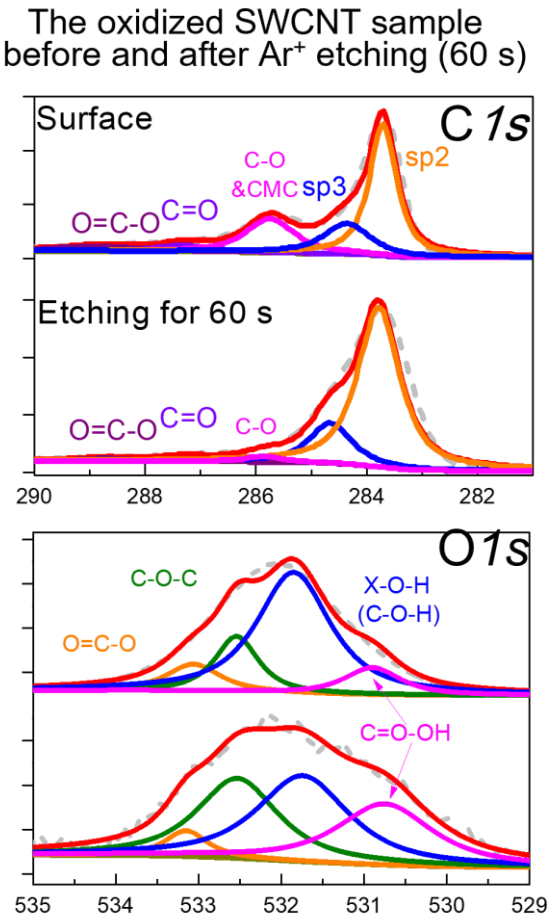

Figure S14 XPS depth profile analysis of C 1s and O 1s of oxidized SWCNT (processed by immersing in 1M $Al(NO_3)_3$ overnight, see Experimental Methods), which was collected at pristine and after etching for 60 s.

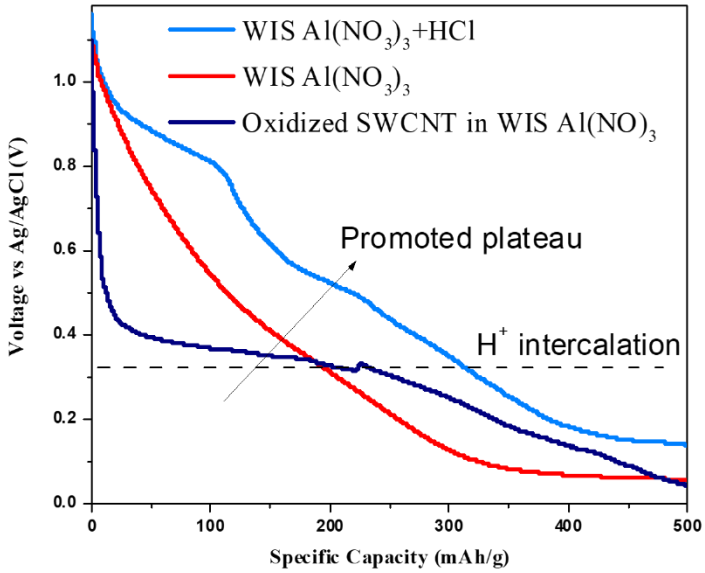

Figure S15 Galvanostatic discharge curves of SWCNT and oxidized SWCNT in WIS-$Al(NO_3)_3$ and WIS-$Al(NO_3)_3$/HCl electrolytes by the 3-electrode system at a current density

of 500 mA g^{-1}. A clear discharge plateau at 0.55 V was found by SWCNT in WIS-$Al(NO_3)_3$/HCl electrolyte, indicating the Cl^- assisted intercalation of Al^{3+}. However, only an obvious discharge plateau at 0.35 V was found by oxidized SWCNT in WIS-$Al(NO_3)_3$ electrolyte due to the enhanced intercalation of H^+ with more oxygen-containing groups. This shows the oxidation of the SWCNT cathode mainly affects the intercalation of H^+ rather than Al^{3+}.

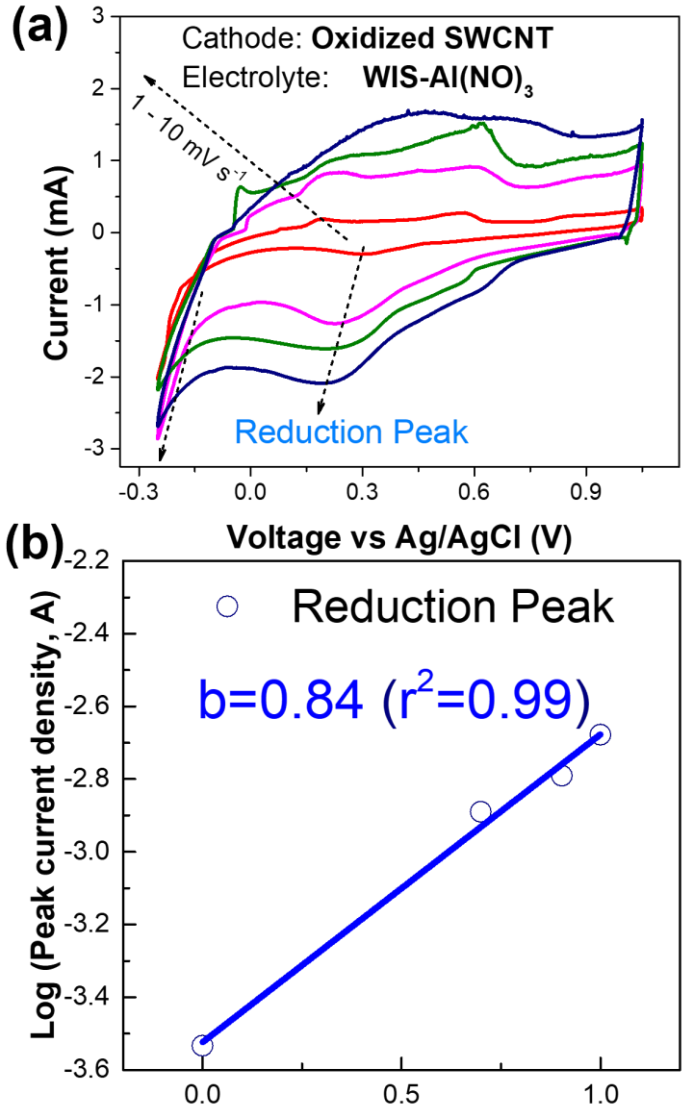

Figure S16 (a) Cyclic voltammetry (CV) of the oxidized SWCNT in WIS-$Al(NO_3)_3$ at a series of scan rates by 3-electrode system and corresponding (b) Linear fitting of log (peak current density) and log (scan rate).

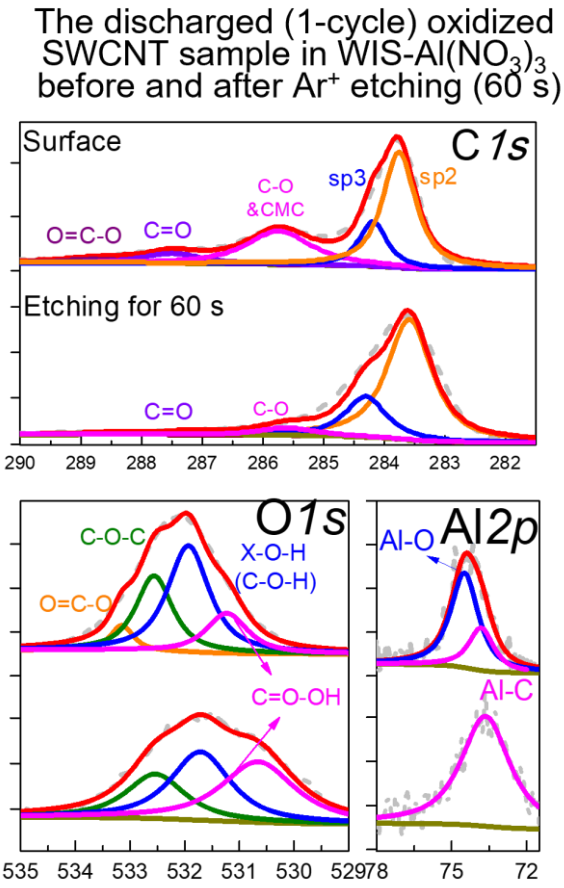

Figure S17 XPS depth profile analysis of C 1s, O 1s and Al 2p of discharged oxidized SWCNT (1-cycle) in WIS-Al$(NO_3)_3$ electrolyte, which was collected at pristine and after etching for 60 s.

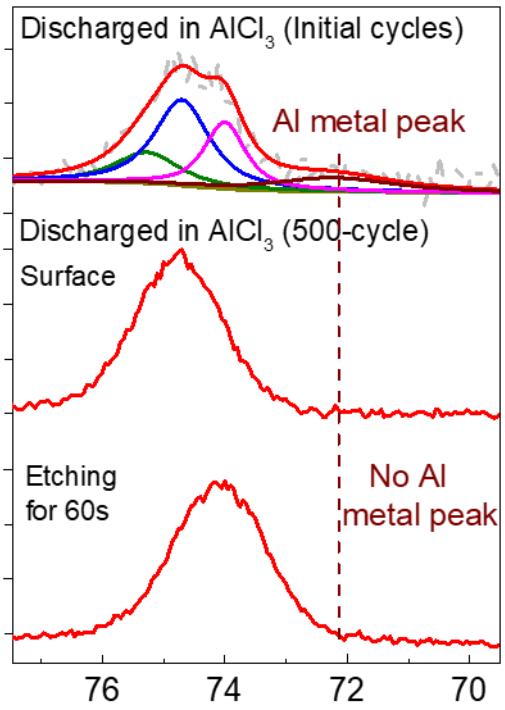

Figure S18 XPS data Al 2p of discharged SWCNT samples at initial cycles and after long-term cycles, where the Al metal peak appears in the discharged sample at initial cycles, while no signal can be seen at the long-term cycled sample, indicating overcharged/over-discharge may cause the over-discharge/overcharge, and thus the reaction $Al_2Cl_7^- \rightarrow Al+AlCl_4^-$ happens on the cathode during initial cycles as the ion balance has not been formed in the electrolyte, resulting in the Al0 peak in the obtained XRD patterns (Figure 4c).

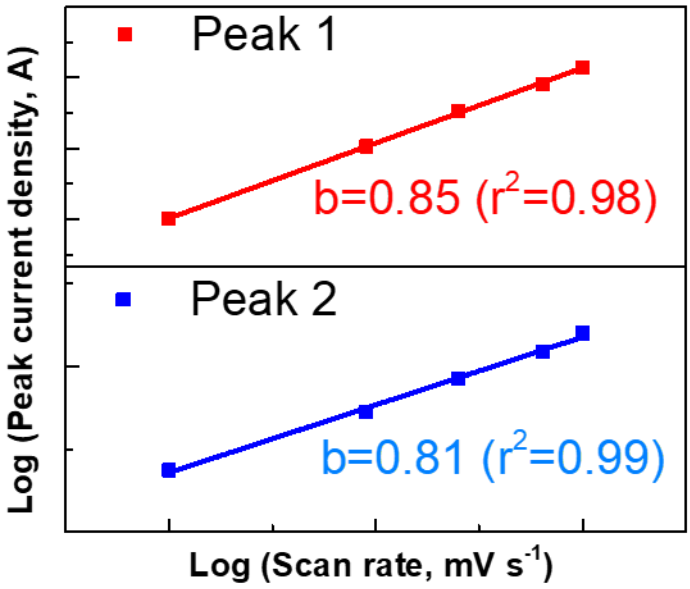

Figure S19 Linear fitting of log (peak current density) and log (scan rate) of the CV curves of SWCNT in WIS-$Al(NO_3)_3$/HCl electrolyte by the 3-electrode system.

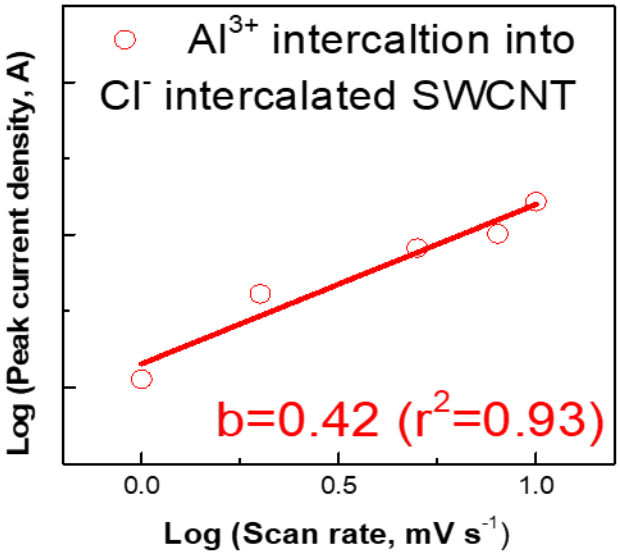

Figure S20 Linear fitting of log (peak current density) and log (scan rate) of the CV curves of Cl-SWCNT in WIS-Al$(NO_3)_3$ electrolyte by the 3-electrode system.

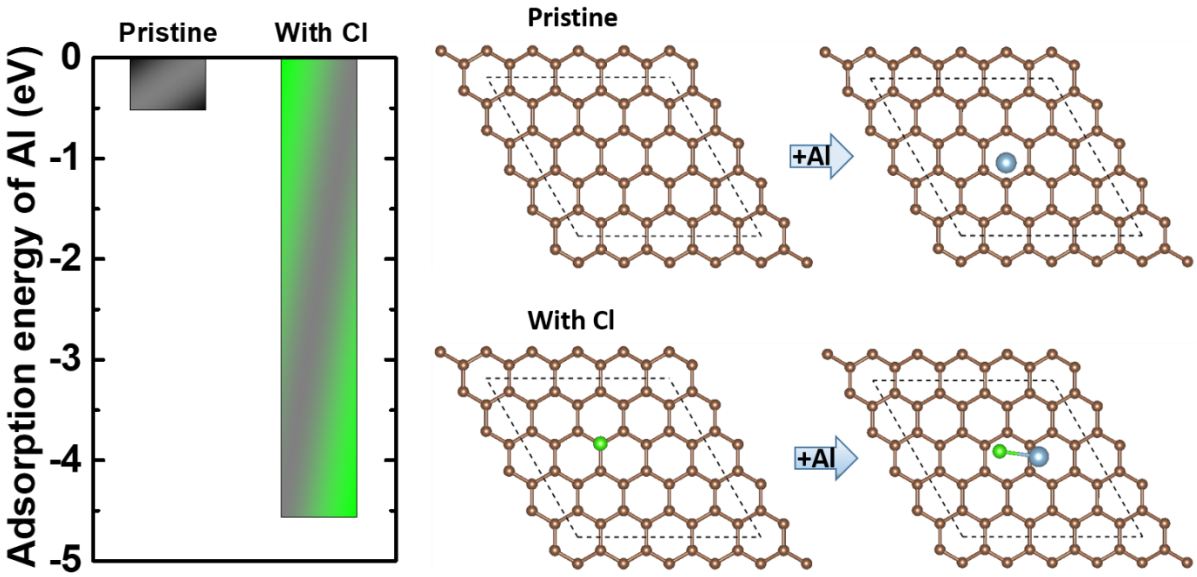

Figure S21 Adsorption energies of an Al atom on pristine and Cl-adsorbed graphene.

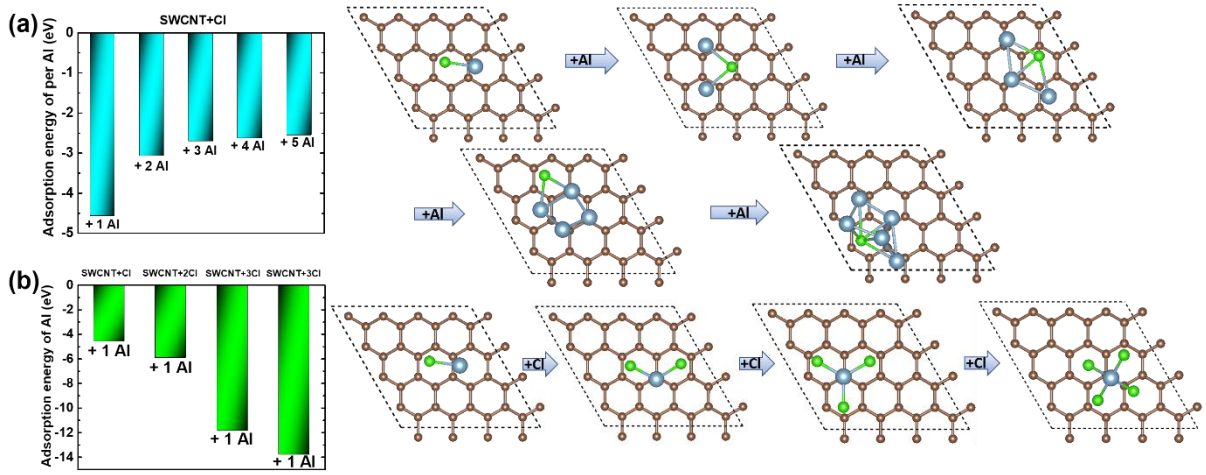

Figure S22 (a) Adsorption energies of an Al atom on multi-Cl-adsorbed graphene and (b) average adsorption energies per Al atom of multi-Al atom on Cl-adsorbed graphene. Interestingly, the energy increased significantly when 3 Cl ions were absorbed on the SWCNT, indicating an Al favourited intercalation state, which may form an intercalation stage similar to the intercalation of $AlCl_4^-$.

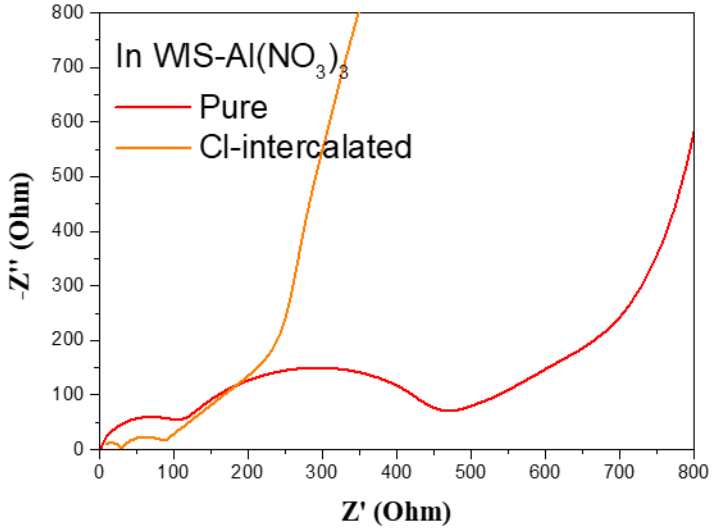

Figure S23 Resistance of pure SWCNT and Cl-intercalated SWCNT in WIS-$Al(NO_3)_3$ electrolyte in 3-electrode system.

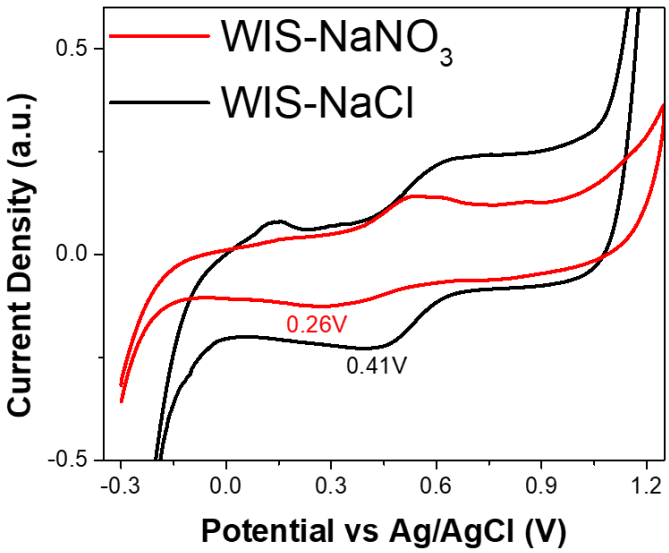

Figure S24 CV curves of SWCNT in WIS-$NaNO_3$ and WIS-NaCl electrolytes in 3-electrode system.

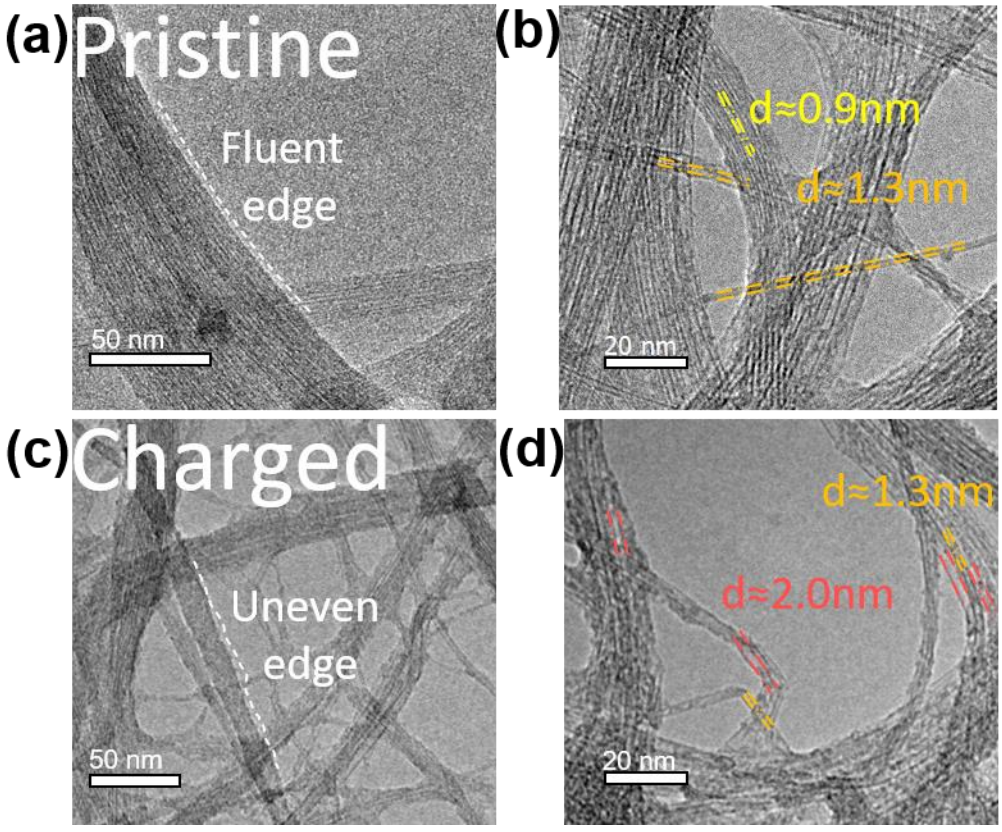

Figure S25 TEM images of SWCNT at (a and b) pristine and (c and d) charged state, where the SWCNT bundles show distorted shape and the interlayer space was enlarged, indicating the intercalation of $AlCl_4^-$.

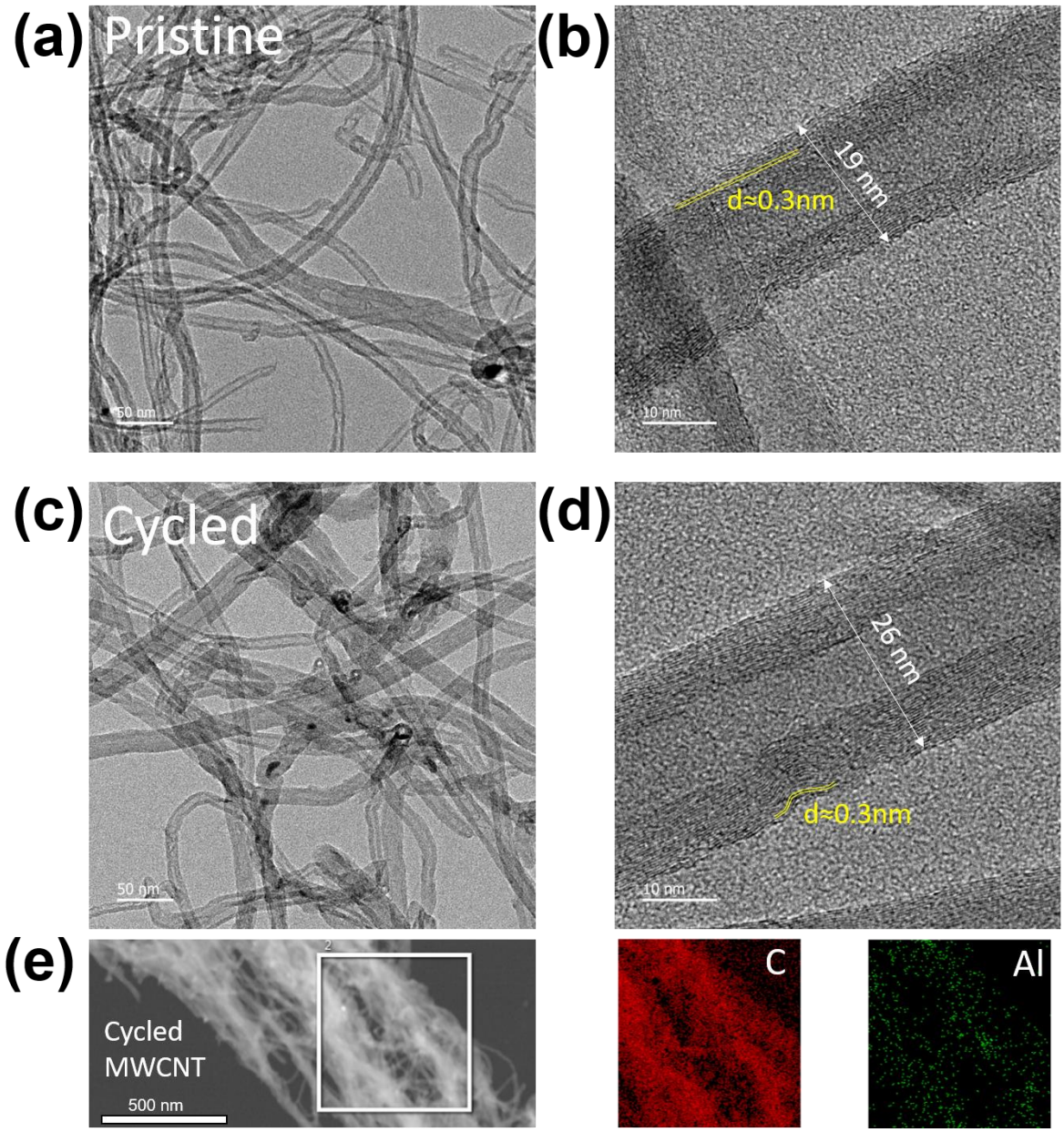

Figure S26 TEM images of MWCNT at (a and b) pristine and (c and d) cycled state and (e) corresponding EDX elemental analysis, where the MWCNT bundles show no change of morphology mostly, indicating only the intercalation of Al^{3+} without $AlCl_4^-$.

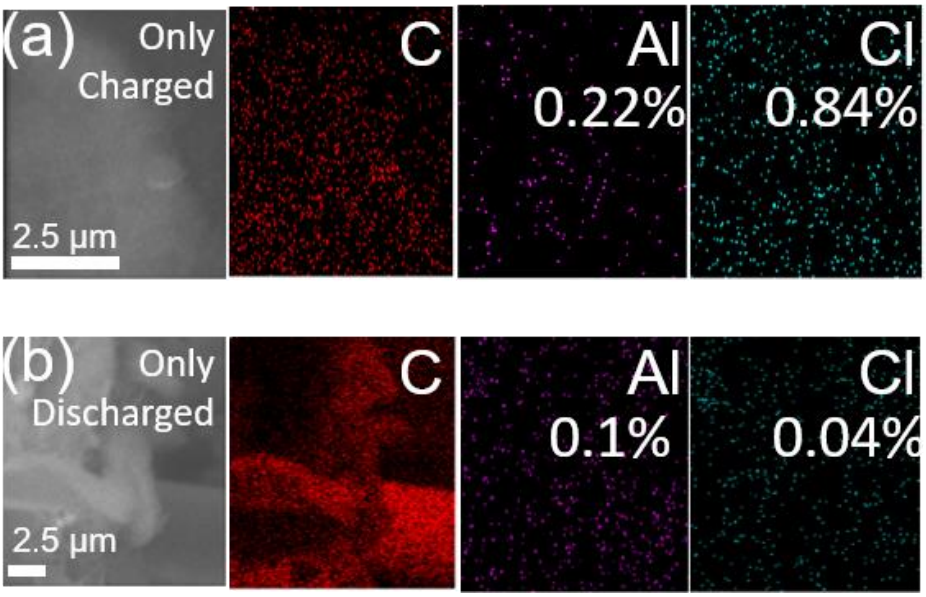

Figure S27 SEM-EDX of SWCNT cathode at first charged and first discharged states. An atomic ratio of 1:4 for Al: Cl was observed on the only charged SWCNT, indicating the intercalation of $AlCl_4^-$, while a low ratio of 1:0.4 was found on the only discharged SWCNT, suggesting the intercalation of Al^{3+} (Residential Cl may be from attached Cl on the surface).

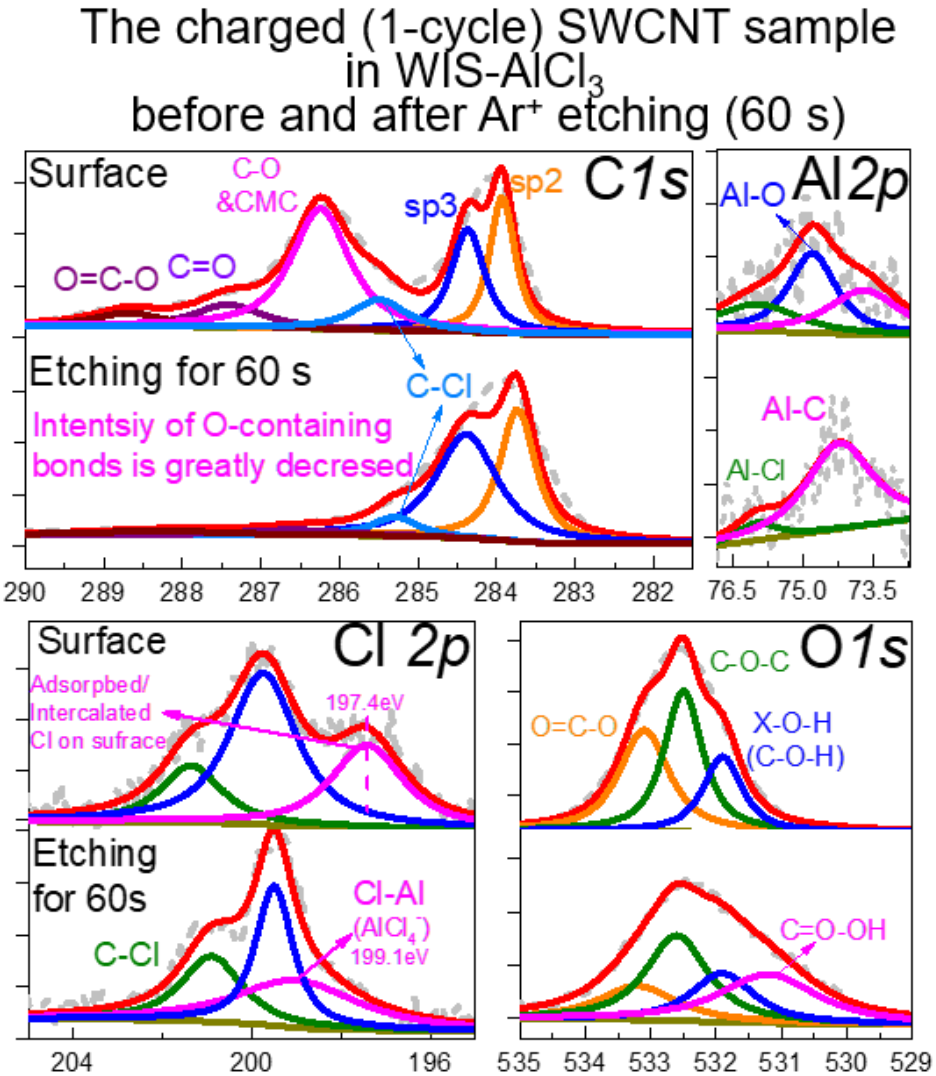

Figure S28 XPS depth profile analysis of C 1s, Al 2p, O 1s and Cl 2p of charged SWCNT (1-cycle) in WIS-$AlCl_3$ electrolyte collected at pristine and after etching for 60 s.

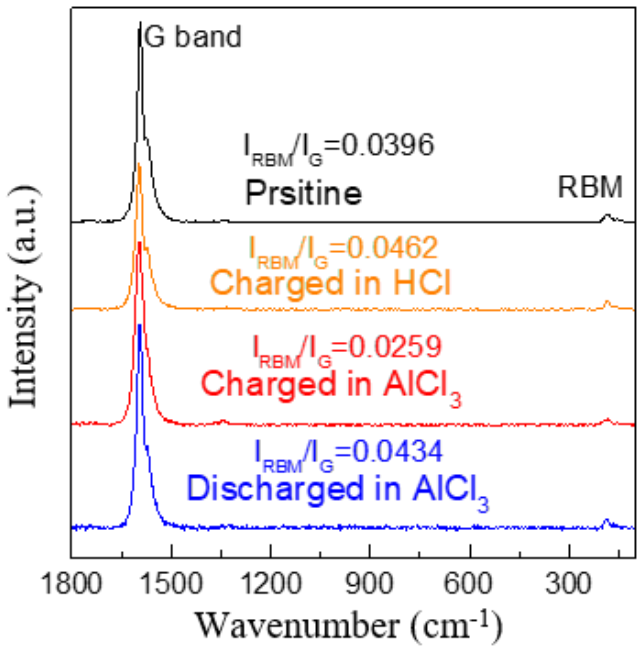

Figure S29 Raman spectrum ranging from 1800 cm^{-1} to 100 cm^{-1}, presenting G band and RBM mode. And ratios of RBM intensity and G band intensity at different stages were also labelled, showing the different aggregation conditions of SWCNTs.

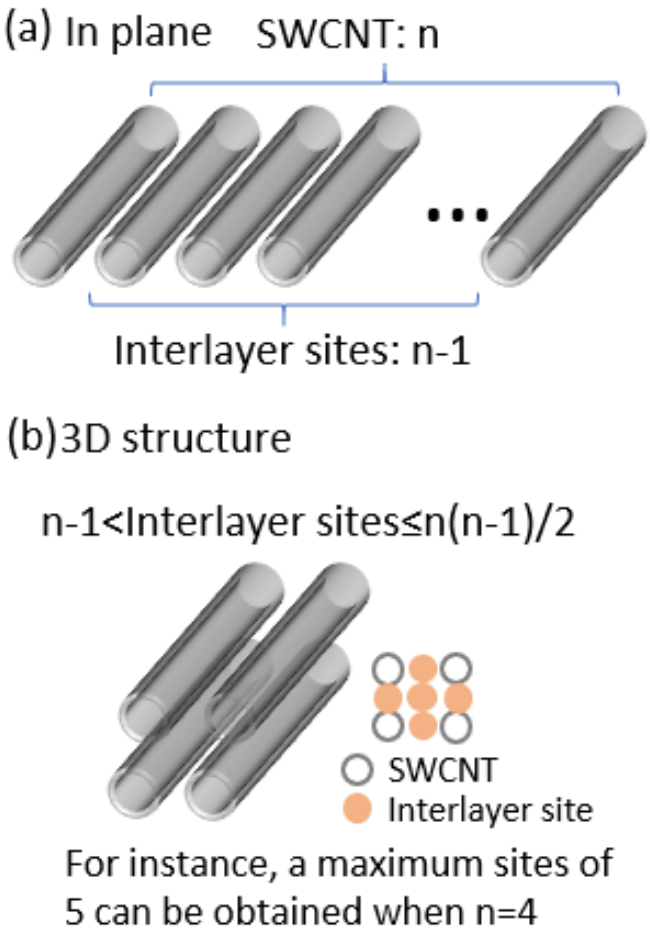

Figure S30 Schematic figures of the interlayer sites of SWCNT bundles in a plane (a) and with 3D structure (b). As an important factor, agglomerate related studies deserve further investigation and optimization in the future. For instance, the SWCNT bundles with n tubes show a maximum interlayer site number of n(n-1) in a plane, which can even be further increased by 3D structure. This suggests that the modification of SWCNT, especially controlling the agglomeration state, can further promote the intercalation capacity of large $AlCl_4^-$ anions.

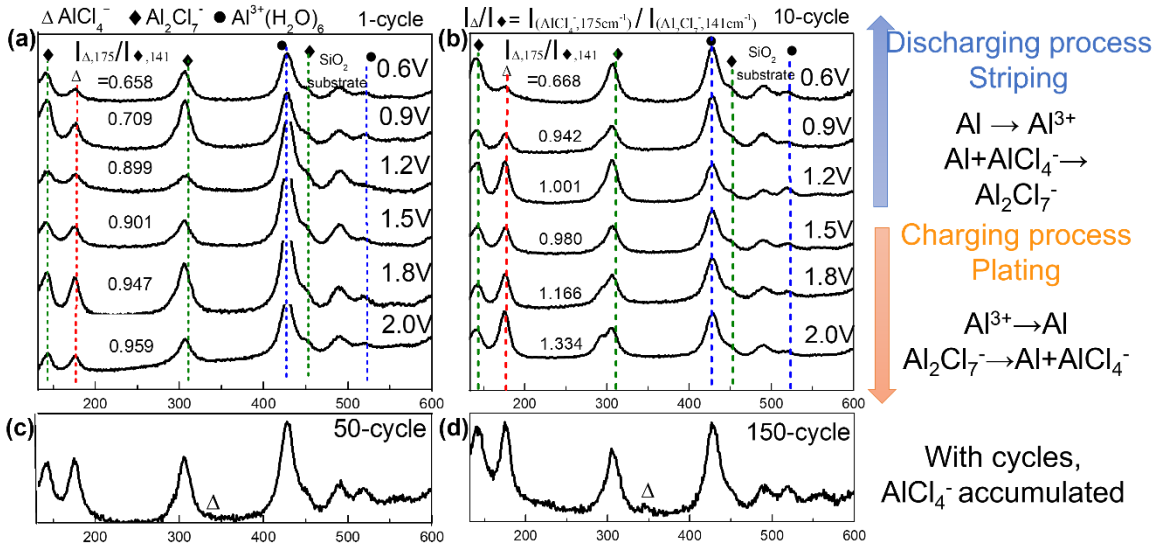

Figure S31 (a-d) Raman spectrum ranging from 132 cm^{-1} to 600 cm^{-1}, presenting the species, such as $AlCl_4^-$, $Al_2Cl_7^-$ and $Al^{3+}(H_2O)_6$, in the WIS-$AlCl_3$ electrolyte at different stages. The ratios of $AlCl_4^-$ and $Al_2Cl_7^-$ at different stages were also labeled by the intensity of the peaks at 175 and 141 cm^{-1}, respectively, showing the different conditions of the WIS-$AlCl_3$ electrolytes. Moreover, the standard peak of $AlCl_4^-$ at 345 cm^{-1} is not easy to observe in the WIS-$AlCl_3$ electrolyte initially due to the different configuration from traditional ionic liquid electrolytes, but occurs after tens of cycles (Figures c and d), indicating the increased amount of $AlCl_4^-$ after some cycles in the activation stage.

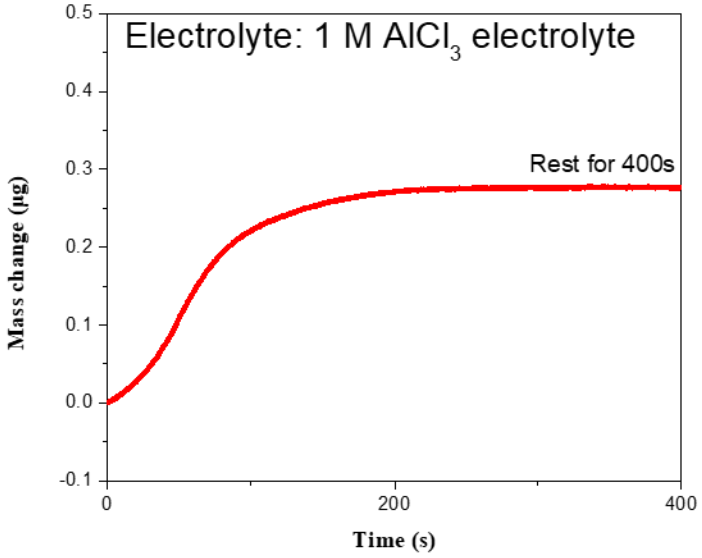

Figure S32 Mass change of SWCNT during the beginning 400 s of the EQCM test in 1M $AlCl_3$ electrolyte, which increased at first 100 s due to some ions attachment and became stable after 200 s, indicating the reliability of the subsequent EQCM measurement.